PREPRINT

tascc

TASCC-P-95-32

DEPENDENCE OF IMF PRODUCTION ON THE REACTION MECHANISM IN LIGHT HEAVY ION COLLISIONS AT INTERMEDIATE ENERGY *

Y. Larochelle[a], L. Beaulieu[a], G. Anctil[a], G.C. Ball[b], D.R. Bowman[b], B. Djerroud[a †], D. Doré[a ‡], A. Galindo-Uribarri[b], D. Guinet[c], E. Hagberg[b], D. Horn[b], R. Laforest[a §], P. Lautesse[c], J. Pouliot[a **], R. Roy[a], M. Samri[a] and C. St-Pierre[a]

[a] *Laboratoire de physique nucléaire, Département de physique, Université Laval, Québec G1K 7P4, Canada*

[b] *AECL, Chalk River Laboratories, Chalk River, Ontario K0J 1J0, Canada*

[c] *Institut de Physique Nucléaire de Lyon, 46 Bd du 11 Novembre 1918, F-69622, Villeurbanne Cedex, France*

CERN LIBRARIES, GENEVA
SCAN-9511126

JW 9547

* Experiments performed at TASCC, Chalk River, Ontario, Canada

† Present address: NSRL, University of Rochester, 271 East River Road, New York, 14627 USA

‡ Present address: Institut de physique nucleaire d'Orsay, B.P. 91406, Orsay Cedex, France

§ Present address: LPC-ISMRA, Université de Caen, B.P. 14050, Caen Cedex, France

**Present address: Hôtel-Dieu de Québec, Département de Radio-Oncologie, Québec, Canada

Submitted to Phys. Rev. C

NOTICE

This report is not a formal publication; if it is cited as a reference, the citation should indicate that the report is unpublished. To request copies our E-Mail address is **TASCC@CRL.AECL.CA.**

Physical and Environmental Sciences
Chalk River Laboratories
Chalk River, ON K0J 1J0 Canada

1995 October

Dependence of IMF Production on the Reaction Mechanism in Light Heavy Ion Collisions at Intermediate Energy *

Y. Larochelle[a], L. Beaulieu[a], G. Anctil[a], G.C. Ball[b], D.R. Bowman[b], B. Djerroud[a] †, D. Doré[a] ‡, A. Galindo-Uribarri[b], D. Guinet[c], E. Hagberg[b], D. Horn[b], R. Laforest[a] §, P. Lautesse[c], J. Pouliot[a] **, R. Roy[a], M. Samri[a] and C. St-Pierre[a]

[a] *Laboratoire de physique nucléaire, Département de physique, Université Laval, Québec, Canada G1K 7P4*

[b] *AECL, Chalk River Laboratories, Ontario, Canada K0J 1J0*

[c] *Institut de Physique Nucléaire de Lyon, 46 Bd du 11 Novembre 1918, F-69622, Villeurbanne Cedex, France*

(October 4, 1995)

---

*Experiments performed at TASCC, Chalk River, Ontario, Canada

†Present address: NSRL, University of Rochester, 271 East River Road, New York 14627, USA

‡Present address: Institut de physique nucleaire d'Orsay, B.P. 91406, Orsay Cedex, France

§Present address: LPC-ISMRA, Université de Caen, B.P. 14050, Caen Cedex, France

**Present address: Hôtel-Dieu de Québec, Département de Radio-Oncologie, Québec, Canada

Abstract

The same hot nuclear system ($\Sigma Z=18$) has been studied for two different entrance channels with reaction products detected in a forward array of scintillators: central collisions of ^{24}Mg on a ^{12}C target at $25A$ and $35A$ MeV and peripheral pick-up reactions of ^{35}Cl on a ^{197}Au target at $43A$ MeV. The detection-efficiency-corrected charge distributions, multiplicity of charged particles and cross sections as a function of excitation energy are compared. The reaction mechanism is investigated, through comparison to simulations with statistical observables. The central reaction $^{24}Mg+^{12}C$ at $35A$ MeV is well characterized by a dissipative binary collision scenario. Data at $25A$ MeV show less evidence of such dynamical characteristics. The IMF ($3\leq Z\leq 8$) production for each reaction is compared to model calculations for different values of excitation energy. The systems formed in the central collision at $25A$ MeV and the pick-up reaction at $43A$ MeV show similar source characteristics, both statistically and in momentum space. However, the yields of the various exit channels, from evaporation/fission to multifragmentation and vaporization, differ for the two reactions.

PACS number(s): 25.70.Gh, 25.70.Kk, 25.70.Mn, 25.70.Pq

I. INTRODUCTION

The multifragmentation [1–4] of hot nuclear systems formed by the collision of heavy ions in the intermediate energy range (between $10A$ and $100A$ MeV) has usually been considered in the context of a thermalized, equilibrated emitting source. Recently, however, there has been an increasing interest in the effects of reaction dynamics on the production of intermediate-mass fragments (IMF, $3 \leq Z \leq 8$) and light charged particles (LCP, Z=1 or 2) [5–14]. In this paper we compare emission from sources of the same mass and charge, in this case A = 36 and Z = 18, produced by two different reaction mechanisms and detected with the same experimental apparatus. The first system is formed in the central collision of ^{24}Mg with ^{12}C at $25A$ MeV and $35A$ MeV, where the total charge of the system is detected and could be reconstructed in the center of mass (CM) frame of the reaction. The second system is produced in the peripheral reaction of ^{35}Cl with ^{197}Au at $43A$ MeV, with pick-up of one proton. The same total charge ($\Sigma Z=18$) is identified as coming from a fast-moving source associated with the moving frame of the quasi-projectile (QP).

Much effort has already been devoted to the projectile break-up reactions observed in peripheral collisions of a relatively light nucleus with a heavier target. These reactions involve the pick-up, exchange or stripping of nucleons [14–26]. Several trends have been identified from these analyses, assuming a thermalized source for the emission of particles. Of particular interest are:

- the statistical and sequential nature of such multifragmentation events [23,26,27],
- the increase of IMF yields with increasing excitation energy of the emitting source [24], and
- the decrease of emission time for LCP with the increase of excitation energy [28,29].

The present paper will deal with similar topics but with special emphasis on the entrance channel and the early stage of the reaction and their effects on the subsequent multifragmentation phenomena. The experimental set-up is described and the calibration methods

presented in Section 2. In Section 3, we make an analysis of the instrumental bias imposed on the data. We also explore the corrections made to permit comparison of experimental yields from different data sets and predicted yields from various models. The cross sections for charge distributions, charged-particle multiplicities, and excitation energy (assuming compound-nucleus formation) are presented. Possible reaction mechanisms are investigated in Section 4, by means of global observables and filtered statistical simulations. In Section 5, the IMF production and exit channel yields for four types of exit channels (heavy residue production, dissipative evaporation/fission, multifragmentation and vaporization) are compared for specific values of excitation energy. Finally, in Section 6, the results are summarized and conclusions are presented concerning the dependence of IMF production on the entrance channel of the reaction.

II. EXPERIMENTAL SETUP AND CALIBRATION

A. The ^{24}Mg+^{12}C experiments

The experiments were performed at the TASCC facility of Chalk River Laboratories, with beams of ^{24}Mg at 25A and 35A MeV incident on a 2.4 mg/cm^2 C target. The inverse-kinematics conditions focussed reaction products into the 80-detector CRL-Laval Array, shown in Fig. 1. The most forward part of the array is composed of three rings of 16 plastic phoswich detectors, covering polar angles from 6.8° to 24° with respect to the beam axis. Each phoswich detector consists of a thick, slow-plastic E detector and a 0.7-mm ΔE layer of fast plastic scintillator, heat-pressed to the front of the E detector [30]. These allowed identification of charged fragments from Z=1 to 12. The set-up is completed with two additional rings, each with 16 CsI(Tl) scintillators, covering the angular range from 24° to 46° for particles of Z=1 and 2. Typical spectra can be found in Ref. [31].

Energy thresholds varied from 7.5A to 19.6A MeV for Z=1 to Z=12 in the phoswich detectors and were approximately of 2A MeV in the CsI(Tl) detectors. Identification of Z=3 particles, with a threshold of less than 5A MeV, and isotopic resolution for Z=1, were achieved by the CsI(Tl) detectors in the 25A MeV experiment. At 35A MeV the masses of Z=1 particles were randomly assigned as $1, 2, 3$ in $60\%, 30\%, 10\%$ ratios, respectively, based on the isotopic yield ratios measured at 25A MeV. For all other fragments the mass was given as $2Z$.

To minimize accidental coincidences, only particles arriving within one cyclotron period (25 ns) were included in an event. Events with two particles striking the same detector were largely eliminated by means of restrictive gates on the charge identification spectra for all the detectors and by a special gate on the α-particle double hit band, which was counted as two α-particles with identical energies, coming from the ground-state dissociation of ^{8}Be. The calculated grazing angles in these reactions are 2.6° and 1.8° for experiments at 25A and 35A MeV respectively (see Ref. [32]).

B. The $^{35}Cl+^{197}Au$ experiment

The experimental setup used in the $^{35}Cl+^{197}Au$ is very similar to the one for $^{24}Mg+^{12}C$ but with some different experimental conditions and additions to the setup. The charge resolution in the CsI(Tl) detectors allowed identification up to Z=4. The phoswich detector gains were adjusted in order to achieve identification up to Z=17. The grazing angle in this reaction is 6.3°, very close to the inner ring of phoswich detectors.

For the present analysis, events with $\Sigma Z=18$, identified as coming from breakup of a quasi-projectile according to systematics from Ref. [33], were used for comparison. More information on projectile break-up event selection can be found in Ref. [34]. In order to minimize the experimental bias in the comparison with the $^{24}Mg+^{12}C$ data, events with a fragment of Z>12 in a phoswich or Z>3 in a CsI(Tl) detector were rejected. Events with "electronic multiplicity" (number of discriminators triggered) ≥ 2, ≥ 4 and ≥ 6 were used for the $^{35}Cl+^{197}Au$ data. In the case of the $^{24}Mg+^{12}C$ reaction, only triggers on electronic multiplicity ≥ 6 were used, mainly because most of the events with $\Sigma Z=18$ analyzed from data of electronic multiplicity ≥ 2 contained six or more charged particles.

C. Calibration and center-of-mass reconstruction

Energy calibration points were obtained from elastically scattered ^{24}Mg ions and secondary beams of Z=1 through 11 scattered on ^{197}Au targets mounted at various distances from the detectors. The phoswich detectors were calibrated with the relation given in Ref. [35] and the CsI(Tl) detectors with the energy-light relation from Ref. [31]. The intrinsic resolution of the detectors was better than 5% and the precision of the energy-light relation close to 5% for both types of detectors.

For the $^{24}Mg+^{12}C$ data, the velocity of the center-of-mass (CM) frame for the reaction products of an event was reconstructed from all the charged particles detected. In the case of the $^{35}Cl+^{197}Au$ data, the moving frame was reconstructed by the same procedure, but

only with particles identified as coming from the decay of the quasi-projectile. As a test of the energy calibration and event characterisation, Fig. 2 shows the reconstructed velocity of the moving source for all three reactions, for completely and incompletely detected events in the central-collision data, and for peripheral collision events in which the total charge of the QP is equal to 18. Two observations can be made from these plots: (i) the bias in the momentum space can be important for incompletely detected events, because they present large fluctuations in the measured CM velocity, and (ii) the velocity of the moving frame of the QP in the peripheral-collision data is higher than the system's CM velocity in the $^{24}Mg+^{12}C$ data. This last point will be important when considering the effect of the detectors' energy threshold on the analysis. In this work, only events with $\Sigma Z=18$ will be retained for the subsequent analysis.

III. EXPERIMENTAL RESULTS

A. Angular distributions and cross section calculations

In order to compare the absolute cross sections from the three reactions, we perfomed a least-squares fit of the angular distributions for each charge, as measured over the detection range (7^o to 46^o for $1 \leq Z \leq 3$ and 7^o to 24^o for $4 \leq Z \leq 12$). The distributions were then extrapolated to 0^o and 180^o, assuming a constant (log scale) slope. The detection efficiency factor for each charge was obtained from the integral of the distributions over the region of detection, divided by the integral over all angles. The detection efficiency for one particular charged-particle exit channel is then defined as

$$\varepsilon_{EC} = \prod_{i=1}^{M} \varepsilon(Z_i) \ , \tag{1}$$

where $\varepsilon(Z_i)$ is the detection efficiency for each particle.

Table I gives the detection efficiencies for charge 1 to 12 in events with ΣZ=18 for both central and pick-up reactions. The efficiency factors used for ^{24}Mg+^{12}C are the same at both energies, except for Z=3, which are not identified in the CsI(Tl) for the 35A MeV experiment.

B. Experimental bias corrections (EBC) for ^{35}Cl+^{197}Au data

Two important biases affect the relative detection rates for complete events from the three reactions: the beam exit port (0^o-6.8^o) and the energy thresholds for fragment detection in the moving frame of the reaction products. Since the CM of the ^{24}Mg+^{12}C system moves at 0^o in the laboratory frame with a velocity of 0.15c (25A MeV) and 0.18c (35A MeV) and the center of mass of the quasi-projectile breakup products from the peripheral pick-up reaction moves, based on our analysis, at an average velocity of 0.23c and an angle of 6^o in the laboratory frame, the 0^o to 6.8^o forward cone (beam hole) has a very different effect on

the two data sets. This effect can not be corrected for the central data, since this would involve generating events which had not been detected.

Instead, we choose to reject that portion of the ^{35}Cl+^{197}Au data which would not have been detected, had it come from a "central collision" source trajectory. We do this by means of an "artificial" beam hole put in the QP trajectory for the ^{35}Cl+^{197}Au data, with an angular aperture chosen to reflect the same bias as for the ^{24}Mg+^{12}C data. The condition imposed on each particle is

$$\theta = tan^{-1}\frac{V_{per}}{V_{par} + V_{CM}(Mg + C)} > 6.8^{o} \ , \tag{2}$$

where V_{par} and V_{per} are the velocity components parallel and perpendicular to the QP trajectory in the QP frame and $V_{CM}(Mg + C)$ is the CM velocity of the ^{24}Mg+^{12}C at 25A MeV system in the laboratory frame.

To take into account the effective energy-threshold differences in the CM frame of each system, the velocity thresholds for all Z values in their respective moving frames were raised to match those for the central data at 25A MeV. With these two corrections, about 60% of the ^{35}Cl+^{197}Au events with ΣZ=18 were rejected. These corrections to the peripheral pick-up data will henceforth be referred to as EBC (experimental bias corrections). The inverse correction, for those complete events detected in a central reaction that would not have been detected if their CM frame were moving at QP velocity, was also considered; however, tests showed no additional experimental bias on the analysis in this case.

By integrating the exit-channel cross section yields, one can get a rough estimate of the effiency-corrected cross section of the detected events. The results are about 20 mb for the ^{24}Mg+^{12}C at 25A MeV data and 40 mb for the ^{24}Mg+^{12}C at 35A MeV data, which is a small percentage of the geometric total reaction cross-section ($\sigma_r[barn] = (0.14)^2\pi(A_{proj}^{1/3} + A_{target}^{1/3})^2$), estimated at 2 barn. The cross-section increase between 25A MeV and 35A MeV may be due to the increased detector acceptance for higher velocities. The same integration gives 800 mb for the ^{35}Cl+^{197}Au at 43A MeV data with the EBC, still a modest fraction of the total cross-section, estimated at 5 barn. Table II gives the cross sections of selected

exit channels for the three experiments.

C. Charge and velocity distributions

Charged-particle cross sections are given in Fig. 3 for central reactions of ^{24}Mg+^{12}C and also the ^{35}Cl peripheral data with and without the EBC. Four remarks can be made from those distributions. First, the cross section yield of the peripheral reactions is about two orders of magnitude larger than that for the central data; however, these are the ΣZ(detected)= 18 yields and should not be confused with the "singles" cross sections. Secondly, the ^{35}Cl+^{197}Au cross sections with EBC are much closer in general shape to the ^{24}Mg+^{12}C yield at 25A MeV than the ^{35}Cl+^{197}Au cross sections without corrections, and show a relative enhancement in IMF production. The Z=2 yield is higher for the central reaction, possibly because of the dominant alpha-cluster structure in ^{24}Mg and ^{12}C [36,37]. Finally we note that the slope of the 35A MeV Z distribution may differ from that at 25A MeV, due in part to the higher energy dissipation at this beam energy and in part to the lack of Z=3 detection in the CsI(Tl) in that experiment.

Figure 4 shows the cross section yields of the laboratory velocity of all charged particles as a function of their charge. The experimental bias due to the detectors' energy threshold can be seen in the plots, especially in the 25A MeV and 35A MeV central data where they are close to the CM velocity. With the EBC applied to the ^{35}Cl+^{197}Au data, the velocity distributions are similar for both reactions.

D. CP multiplicity and excitation energy distributions

The multiplicity of charged products and the excitation energy of the emitting source are two valuable observables characterizing a hot nuclear system. Before comparing the reaction mechanisms for the different systems, let us examine these observables.

Cross sections of charged-particle multiplicity for the three data sets are displayed in Figure 5. Again, the corrected data set for the peripheral pick-up reaction is closer to the

central 25A MeV data, averaging a charged-particle multiplicity of 7. The low yield of charged-particle multiplicity of 5 or less in the central-collision data can be explained by the fact that only runs of "electronic multiplicity"$\geq$6 were used for this analysis.

To extract the excitation energy (E^*) for each event, the velocity of the moving frame of the reaction products is reconstructed and the relative velocites, v_i, of the particles are used to obtain the relative kinetic energy K_{rel} in the CM frame of the reaction products. The Q value ($Q_0 < 0$) of the reaction channel is calculated from the experimental particle mass and assuming an $^{36}Ar^*$ entry channel, the excitation energy is given by $E^* = K_{rel} - Q_0$. If the total reconstructed mass is less than 36, a correction for neutrons is then caculated, as in Ref. [15].

The resulting excitation energy distributions are displayed in Figure 6. For the central data, the distribution are peaked near the CM fusion value of 200 MeV for the 25A MeV reaction and 280 MeV for the 35A MeV reaction. The large width of the E^* spectra around the mean value is mainly due to the detector acceptance and incorrect estimates of particle mass and energy. This broadening is reproduced by "filtered" simulations with a unique excitation energy input value, as discussed in the next section.

For the peripheral data, the EBC procedure selects exit channels of higher excitation energy, yielding more intermediate-mass fragments (Fig. 3) and higher multiplicities (Fig. 5). The similarities, for those observables, between peripheral data with EBC and central data suggest possible comparisons between the different data sets. The excitation energy spectrum of the ^{35}Cl+^{197}Au system with EBC covers a large range of energies, as one would expect for a peripheral collision [23,24,26]. It peaks around the same value as the narrower distribution of ^{24}Mg+^{12}C at 25A MeV (about 200 MeV, or 5.6A MeV), and still has a large yield around 300 MeV, or 8.3A MeV, which corresponds to the region covered by the distribution for the ^{24}Mg+^{12}C reaction at 35 MeV. This large range will be useful, allowing us to make cuts on E^* for comparison with the other sets of data and with simulations.

IV. REACTION MECHANISMS

A. GEMINI simulations

The events selected with $\Sigma Z=18$ were compared to simulations generated with the statistical code GEMINI [38] and filtered by the detector acceptance. The angular momentum input to the code was determined from a comparison between experimental data and simulations made for different values of angular momentum. For the limiting case corresponding to the complete fusion of projectile and target, we examined an angular momentum observable [33], which gives the angle between each particle velocity and the reaction plane normal (deduced from the trajectory of the heaviest fragment), for Ar^* with angular momentum values of 0, 8, 17 or 25 $\hbar$. The angular momentum observable showed that the best agreement with the data was obtained for the calculated maximum angular momentum that can be sustained by the nucleus (25 $\hbar$ for argon), as determined from formulations in Ref. [39]. A single angular momentum value was used for all generated events in a given simulation.

Four such simulations were generated. In each case the excited nucleus was ^{36}Ar, corresponding to the two $^{24}Mg+^{12}C$ experiments assuming fusion, and to two excitation ranges for the peripheral $^{35}Cl+^{197}Au$ data. Table III gives the details on the excitation energy and kinematic properties of the argon nucleus in the simulations. The disintegrations simulated with GEMINI were transformed into the laboratory frame and were then passed through the experimental filter reproducing the geometry and energy thresholds of the multidetector array and eliminating neutrons. The filtering also took into account the angular uncertainty due to the solid angle of each detector. The mass assigned to each particle was equal to $2Z$, except for hydrogen where it was randomly distributed as 1, 2, or 3 in a 6:3:1 ratio.

EBC corrections were performed on simulations B and D ($^{35}Cl+^{197}Au$ at $43A$ MeV) in order to compare all simulations and experimental data with the same bias. Z=3 particles were accepted in the CsI(Tl) detectors for simulations A and B but not for simulations C and D, as was the case in the actual $^{24}Mg+^{12}C$ at $35A$ MeV experiment. The same cut

was made on the $^{35}Cl+^{197}Au$ at 43A MeV data only when comparing distributions in this energy range. In this range, the cut affects 13% of all the experimental events and 28% of the events with one or more Z=3 particles. In all simulations, the number of events was chosen in order to get filtered statistics similar to those of the experimental data (at least 5000 events). This represents simulations of more than 1000000 events for cases A and C ($^{24}Mg+^{12}C$) and 100000 events for cases B and D ($^{35}Cl+^{197}Au$). The simulated cross section distributions were renormalized to the experimental results for a scale in mb.

Figure 7 shows the reconstructed excitation energy spectra for all four simulations, done in the same way as for the experimental data, as described in section III D. In all cases, even when a single starting value of E^* was used in the simulations, the filtered E^* distributions are as broad as the experimental ones. It has been verified, by bypassing the experimental filter, that this broadening was a consequence of the detector acceptance and the procedure for deducing particle mass and energy.

B. Anisotropy ratio

Since the deexcitation mechanism in the simulations is based on the sequential and statistical decay of a single, thermalized emitting source, we have to look for similar characteristics in the experimental data before attempting to compare the reaction mechanism and the IMF production for different channels (section V). The first step in the analysis is to determine the characteristics of that source, whether it be a compound nucleus or a quasi-projectile, for all different entrance channels.

A mid-rapidity charge parameter (Z_{mr}) [40] was used to evaluate the centrality of the detected $^{24}Mg+^{12}C$ events. At 25A MeV, 69% of the events had Z_{mr} greater than 15 and at 35A MeV the corresponding fraction was 62% , indicating the violence of the majority of the (ΣZ=18) events. Another way to probe the violence of a collision is to extract the ratio between the total transverse energy of a given event and the total energy available in CM frame of the reaction, for each beam energy. For the completely detected events, that ratio

averaged 0.28 at 25A MeV and 0.27 at 35A MeV, indicating that for the majority of these events more than 25% of the CM energy is transverse to the beam.

The high energy thresholds of the phoswich detectors for heavy fragments (Z>6) excludes the use of forward/backward asymmetry as a criterion to discriminate between the different reaction mechanism scenarios. On the other hand, the elongation of an event in momentum space can be used for distinguishing between binary and compound-nucleus reaction mechanisms. Quantitatively, a global variable can be constructed from a comparison of the longitudinal and transverse momentum components of the event's constituent particles [41]. This anisotropy ratio, R_A, is defined as

$$R_A = \frac{2}{\pi} \frac{\sum_{i=1}^{M} |P_{iCM\perp}|}{\sum_{i=1}^{M} |P_{iCM\parallel}|} , \tag{3}$$

where $\frac{2}{\pi}$ is a geometric normalisation constant, M is the charged-particle multiplicity, and $P_{iCM\parallel}$, $P_{iCM\perp}$ are momenta of the i^{th} particle in the CM frame, parallel and perpendicular to the beam axis. This global variable does not require a determination of the reaction plane, which can be a difficult procedure for such a light system.

Fig. 8 and 9 show anisotropy ratio distributions compared to filtered simulations, for both beam energies of the central ^{24}Mg+^{12}C reactions and for the peripheral ^{35}Cl+^{197}Au collisions. When restricted to events with E*=170-230 MeV (Fig. 8), the central 25A MeV ^{24}Mg+^{12}C and peripheral ^{35}Cl+^{197}Au data sets and simulations are quite similar, though there is some discrepancy between experiment and simulation in the "central fusion" scenario. For events with E*=250-310 MeV (Fig. 9), the central 35A MeV data are different from both the projectile breakup data and the simulations. This may indicate that complete fusion is not an important component of the reaction mechanism for 35A MeV ^{24}Mg+^{12}C collisions.

C. Anisotropy ratio and charged-particle multiplicity

In this section, the possibility of a dissipative binary mechanism is investigated for the ^{24}Mg+^{12}C reaction, by looking at the correlation between two global observables, R_A and

charged-particle multiplicity. Two extreme excitation scenarios were considered: complete fusion, in which the projectile and the target form a thermalized compound nucleus, and binary dissipative collisions, in which a two-source system is produced, composed of a quasi-projectile and a quasi-target with different kinematic and energetic characteristics. In the simulations of dissipative binary collisions, the excitation energy and scattering angle of both the quasi-projectile and the quasi-target were provided by a semi-classical coupled-channels (nucleon exchange) code, TORINO [42].

Anisotropy distribution are plotted in Fig. 10 as a function of charged-particle multiplicities for experimental events with ΣZ=15, 16 or 17, and for experimental and simulated events with ΣZ=18 at 25A and 35A MeV. The effect of the experimental acceptance on the anisotropy ratio distributions can be compared to the horizontal lines representing the R_A distributions for unfiltered simulations, averaged over all multiplicities. Isotropic events should have a mean R_A value of 1.0 for events of very large multiplicity, but for the low multiplicities typical of these reactions, intrinsic fluctuations produce slightly different values of R_A [43] for nearly isotropic events, such as those expected from the complete fusion simulations. It is important to note that the R_A distributions are skewed about their centroids and that the widths of the distributions vary. Consequently, the experimental acceptance may highlight the difference between two distributions having similar unfiltered centroids, as is the case in the 25A MeV simulations.

The anisotropies as a function of multiplicity are found to be similar for the incompletely detected (ΣZ=15, 16, or 17) and completely detected (ΣZ=18) events. For the complete events the anisotropy ratios lie close to the values predicted by the dissipative binary simulation at all multiplicities. Of particular interest is the dependence of R_A upon beam energy. Clearly, at 35A MeV, the anisotropy values deviate more from the fusion predictions than at 25A MeV. This suggests that, as beam energy increases, the two sources become increasingly separated in velocity space.

The code TORINO requires an impact parameter value as input, from which it deduces the subsequent evolution of the reaction. For systems as light and energetic as those reported

here, this should not necessarily be taken as the geometric trajectory of the entrance channel, but rather as a relative scale for the violence of the interaction. The impact parameter that best reproduces the anisotropy ratios at 25A MeV gives excitations of 95 and 81 MeV and velocities of 74% and 57% of the projectile velocity for the projectile-like and target-like sources, respectively. At 35A MeV, the best agreement corresponds to excitation energies of 145 and 98 MeV, and velocities of 76% and 51% of the projectile velocity. Although the binary scenario is a better fit with this observable for both experiments, the central data at 25A MeV are still very close to the fusion scenario; the difference is more important at 35A MeV. Similar conclusions were drawn from the analysis of source-velocity ratios when investigating the 9-He exit channel of this reaction at the same energies [44].

D. Anisotropy and kinetic energy ratio

A global observable that can be used as a statistical decay signature of a reaction is the kinetic energy fraction ratio (R_K) [45,46]. It is given by

$$R_K = \frac{K_{rel}}{K_{rel} - Q_0} = \frac{K_{rel}}{E^*} \ . \tag{4}$$

For the mass range of the systems in analysed in this paper, the approximation $< -Q_0 >$=2T is reasonable. Based on the relation $< K_{rel} >= 2\sqrt{E^*/mass}$ =2T, R_K should average 0.5 for events involving a statistical decay process.

Fig. 11 and 12 show two-dimensional plots of anisotropy versus kinetic energy ratio for events in the excitation energy range of the central 25A MeV reaction (Fig. 11) and of the central 35A MeV reaction (Fig. 12). For each excitation energy range, the ^{24}Mg+^{12}C and ^{35}Cl+^{197}Au data are shown, along with the "central", "peripheral", and "unfiltered" GEMINI simulations. As expected, the unfiltered GEMINI simulations average 0.5 at both energies. Table IV gives the mean value and variance, σ^2, of the R_A and R_K distributions for all sets of data and simulations. Figure 13 shows the differences between the mean values of the data and the simulations. For clarity, the difference is given in χ^2 units, where

$$\chi^2 = (\frac{< R_{exp} > - < R_{sim} >}{\sqrt{\sigma^2_{exp} + \sigma^2_{sim}}})^2 \ . \qquad (5)$$

The deviations from the statistical simulations are more important for the central reaction (open and filled circles). The difference goes up to χ^2=0.5 for R_A and χ^2=1.3 for R_K in the central reaction at 35A MeV. Again this is the sign of a different, non-statistical or dynamical reaction mechanism for the ^{24}Mg+^{12}C reaction, especially at 35A MeV, while the quasi-projectile breakup reactions are clearly statisical, both in their isotropy and in their chemical equilibrium.

E. Incomplete fusion and GENEVE simulations

Incomplete fusion reactions are largely eliminated from our analysis on central reactions by the ΣZ=18 requirement. It has been shown [47,48] that in incomplete fusion reactions produced in reverse kinematics, the pre-equilibrium emission of target-like spectators is not forward-peaked in the laboratory frame. Since the probability is very low that all pre-thermalisation, target-like charged particles are emitted forward of 46^o and above detector thresholds, we do not detect incomplete fusion reactions as complete events. Similarly, pre-equilibrium emission of projectile-like spectators, though rare in reverse kinematics reactions, would be very forward-peaked, and mostly lost in the beam-exit port of the array.

Simulations of incomplete fusion reactions were done with the code GENEVE [49] for the ^{24}Mg+^{12}C system at 35A MeV. The first stage of the code deals with pre-equilibrium emission of projectile-like and target-like protons and neutrons. In the dissipation stage, for small impact parameters, the code assumes a complete damping of the initial relative motion between the two nuclei and the formation of a thermalized compound nucleus (incomplete fusion). For larger impact parameters, it shares the excitation energy between the projectile-like fragment (PLF) and the target-like fragment (TLF), according to their relative masses. The deexcitation phase is similar to that followed by the code GEMINI.

Fig. 14 shows the parallel versus perpendicular velocity of pre-equilibrium (target-like

and projectile-like) proton emission for such a mechanism. As seen in the figure, most pre-equilibrium particles are eliminated by the geometric and energy thresholds of the detector arrays. Since Fig. 14 shows that some incomplete fusion events can be detected, an analysis of R_A versus charged-particle multiplicity has been done. The results are compared to ^{24}Mg+^{12}C at 35A MeV data and presented in Fig. 15. The detected incomplete fusion events are very similar to the complete fusion simulations done with GEMINI in section IV C. The events with one PLF and one TLF are closer to the experimental data. The total GENEVE simulation results in a correlation between charged-particle multiplicity and R_A that have a trend opposite to that of the data. The unfiltered incomplete fusion simulations average R_A=0.85, a lower anisotropy ratio than that for the complete fusion simulations in Fig. 10. The difference is a result of the pre-equilibrium proton emission. From these results, we conclude that incomplete fusion does not appear to be the explanation for the anomaly in the reaction mechanism of ^{24}Mg+^{12}C at 35A MeV.

V. IMF PRODUCTION MECHANISMS

A. Exit channels and IMF cross sections

In Table II, cross sections for 25 exit channels, selected out of a possible 354 for ^{36}Ar with Z=1 to 12, are compared for the different sets of data. Since the cross sections differ by up to two orders of magnitude between central and peripheral data, no direct comparisons can be made between the two reaction mechanisms; however, the ratio of cross sections between two exit channels within the same set of data can be compared. Such ratio comparisons show some similarities between the different sets of data but also large differences that should not appear when two similar thermalized systems are formed in the same excitation energy range. For example, taking the exit channel C + 5He + 2H as a reference (since it has one of the highest cross sections for all the reactions investigated here), we find the cross section ratio for the exit channel F + 4He + H is 1:5 for central data at 25A MeV and 1:4 for peripheral data at 43A MeV. However the ratio for the channel C + B + 3He + H is 1:9 for central data at 25A MeV and 1:2 for peripheral data at 43A MeV. For the 9He channel, the difference is even more extreme: 1:6 for central data at 25A MeV and 1:70 for peripheral data at 43A MeV. These variations in relative yields of specific exit channels for systems of the same size and excitation energy point toward an influence of the early dissipative stage of the reaction on the production of intermediate-mass fragments and light charged particles.

Instead of comparing cross sections for specific exit channels, another measure of the IMF production mechanism involved in a reaction decay is to extract the average number of fragments, ($<M_{IMF}>$), for all exit channels. Figure 16 shows this observable as a function of excitation energy (within a specific range) for the ^{24}Mg+^{12}C and ^{35}Cl+^{197}Au reactions and the corresponding GEMINI simulations.

For the 25A MeV ^{24}Mg+^{12}C data and the ^{35}Cl+^{197}Au data in the E^* range of 170 to 230 MeV (E_{CM}(Mg+C)=200 MeV), the average number of intermediate-mass fragments for

the two simulations, including the effects of filtering, is very close at $<M_{IMF}>$=1.6. The experimental results for the central and peripheral reactions are also close to $<M_{IMF}>$=1.6 but differ from each other by somewhat more than statistical fluctuactions.

For the 35A MeV ^{24}Mg+^{12}C data and the ^{35}Cl+^{197}Au data in the E^* range of 250 to 310 MeV (E_{CM}(Mg+C)=280 MeV), the difference between the two reactions mechanisms is noticeably larger. The underprediction of multifragmentation by the code GEMINI in comparison to the ^{35}Cl+^{197}Au at 43A MeV data has been observed for heavier systems in the same beam-energy range and linked to the absence of dynamical expansion in the calculation [50]. The difference between the two sets of experimental results suggest a dependence of the IMF production rate on the reaction mechanism.

B. Yields of exit channels for heavy residues, evaporation/fission, multifragmentation and vaporization

A more detailed comparison of the decay channels for the different reaction mechanisms was achieved by grouping the exit channels in four basic categories, rather than referring to the channels for specific elements:

1. Heavy residue production, where one heavy fragment (Z> 8) or one heavy fragment and one IMF are detected along with light charged particles (Z=1 or 2).

2. Evaporation from products of a dissipative collision or fission, where one or two IMF are detected with no heavy residue.

3. Multifragmentation, where more than two IMF are detected.

4. Vaporization, where the entire system disintegrates into light charged particles.

Figure 17 shows the cross sections for these different sub-groups for the central 25A-MeV ^{24}Mg+^{12}C data and the peripheral ^{35}Cl+^{197}Au data at 43A MeV with EBC, for 170 $\leq E^* \leq$ 230 MeV, along with the corresponding filtered and unfiltered GEMINI simulations. The

effect of the experimental bias can be evaluated in a comparison the filtered and unfiltered simulations. The central ^{24}Mg+^{12}C data show a higher yield of vaporization events than the simulations or the ^{35}Cl+^{197}Au data. On average, an experimental "vaporization" event is composed of 20% Z=1 and 80% Z=2 particles. In the case of the peripheral pick-up data, the relative yields are remarkably close to the statistical simulations. Thus, even if the analysis in section IV shows that the emitting source closely resembles a thermalized argon nucleus for both reactions, the reaction mechanism in the ^{24}Mg+^{12}C data has a definite influence on the IMF production.

In the case of the central ^{24}Mg+^{12}C data at 35A MeV, with $250 \leq E^* \leq 310$ MeV, Figure 18 shows a very high yield of vaporization, composed of 30% Z=1 and 70% Z=2 particles, compared with the filtered fusion simulations. This is also much higher than the vaporization observed in the ^{35}Cl+^{197}Au quasi-projectile breakup data for the same excitation.This may be taken as another sign of the dynamical or binary nature of the ^{24}Mg+^{12}C data. As discussed previously, in this excitation energy range, the peripheral data also tend to deviate from the GEMINI simulations and show a higher yield of multifragmentation.

VI. CONCLUSION

In this paper, we have investigated the dependence of the final breakup process upon the entrance channel dynamics of a reaction. On the technical side, we have demonstrated, by means of reconstructed source velocity distributions, the validity of our energy calibration and the importance of using only completely detected ($\Sigma Z=18$) events. The need for experimental bias corrections to the peripheral $^{35}Cl+^{197}Au$ data before comparison with central $^{24}Mg+^{12}C$ was explained and evaluated. From the analysis of various distributions, it is clear that the experimental bias for reverse kinematics reactions and the experimental bias *correction* (EBC) for projectile break-up reactions serve to select multifragmentation events. The similarities in charged-particle cross sections, multiplicities, and excitation energies between Z=18, A=36 nuclei formed in $^{35}Cl+^{197}Au$ reactions at 43A MeV (after EBC) and in $^{24}Mg+^{12}C$ reactions at 25A MeV were used as a basis for comparisons in the subsequent analysis.

We have assessed the statistical aspects of the $^{24}Mg+^{12}C$ reactions at 25A and 35A MeV and the $^{35}Cl+^{197}Au$ reaction at 43A MeV by comparing global observables such as anisotropy and kinetic energy ratios to simulations of a thermalized compound nucleus. The peripheral $^{35}Cl+^{197}Au$ at 43A MeV pick-up data show clear statistical characteristics. Apparently, no thermalized compound nuclei are formed in the $^{24}Mg+^{12}C$ at 35A MeV reaction and a dissipative binary mechanism is present. The same reaction at 25A MeV displays less dynamical characteristics. We have demonstrated the statistical nature of the IMF production in $^{35}Cl+^{197}Au$ at 43A MeV with E^* around 200 MeV (5.6 MeV/nucleon). The discrepancy in IMF production cross sections between $^{24}Mg+^{12}C$ at 25A MeV and corresponding statistical simulations was attributed to the reaction mechanism. At higher excitation energy, around 280 MeV (7.8 MeV/nucleon), reaction dynamics, such as binary mechanisms and possibly also compression/expansion, seem necessary to characterize the IMF production for both the central and the peripheral pick-up reaction.

Remaining questions concern the determination of the nature of the non-statistical and

binary reaction mechanism in the $^{24}Mg+^{12}C$ data, possibly through comparisons with a model that treats the dynamics of source formation as well as pre-equilibrium emission and the subsequent statistical decay. New experiments with heavier systems and total charge detection might shed new light on the phenomena. Finally we think there is a need for more experimental results to investigate the entrance-channel dependence of the formation and deexcitation of hot nuclear system and the production of intermediate-mass fragments over a large range of masses and energies.

ACKNOWLEDGMENTS

We would like to thank R.J. Charity and J.-P. Wieleczko for the use of their statistical codes. This work was supported in part by the Natural Sciences and Engineering Research Council of Canada.

REFERENCES

[1] L.G. Moretto and G. Wozniak. Ann. Rev. Nucl. Phys., (1993) and refs therein.

[2] J.A. Lopez and J. Randrup. Nucl. Phys. **A503** , (1989) 183, **A512** , (1990) 345, **A571** , (1994) 379.

[3] D.H.E. Gross. Rep. Prog. Phys. **53**, (1990) 605.

[4] B. Tamain. Enrico Fermi School, Course CXII, Italy 1989, Elsevier Science Publishers B.V., North-Holland, (1991).

[5] D. Jouan, B. Borderie, M.F. Rivet, C. Cabot, H. Fuchs, H. Gauvin, C. Grégoire, F. Hanappe, D. Gardes, M. Montoya, B. Remaud, and F. Sebille. Z. Phys. A **340**, (1991)63.

[6] B. Lott, S.P. Baldwin, B.M. Szabo, B.M. Quednau, W.U. Schröder, J. Tóke, L.G. Sobotka, J. Barreto, R.J. Charity, L. Gallamore, D.G. Sarentites, and D.W. Stracener. Phys. Rev. Lett. **68**, (1992) 3141.

[7] M. Colonna, N. Colonna, A. Bonasera, and M. DiToro. Nucl. Phys. **A541**, (1992) 295.

[8] J. Suro, Y.D. Chan, J.A. Scarpaci, R.G. Stokstad, K. Möhring, and T.C. Schmidt. Nucl. Phys. **A548**, (1992) 353.

[9] R. Wada, M. Gonin, M. Gui, K. Hagel, Y. Lou, D. Utley, B. Xiao, D. Miller, J.B. Natowitz, D. Fabris, G. Nebbia, R. Zanon, B. Chambon, B. Cheynis, A. Demeyer, D. Drain, D. Guinet, X.C. Hu, C. Pastor, K. Zaid, J. Alarja, R. Bertholet, A. Giorni, A. Lleres, C. Morand, P. Stassi, L. Schussler, B. Viano, and P. Gonthier. Nucl. Phys. **A548**, (1992) 471.

[10] C. Schwartz, H. Fuchs, H. Homeyer, K. Möhring, T. Schmidt, A. Siwek, A. Sourell, W. Terlau, and A. Budzanowski. Z. Phys. A **345**, (1993) 29.

[11] G. Peilert, H. Stöcker, and W. Greiner. Rep. Prog. Phys. 57, (1994) 533.

[12] J.F. Lecolley, L. Stuggé, M. Aboufirassi, A. Badala, B. Bilwes, R. Bougault, R. Brou, F. Cosmo, J. Colin, D. Durand, J. Galin, A. Genoux-Lubain, D. Guerreau, D. Horn, D. Jacquet, J.L. Laville, F. Lefebvres, C. LeBrun, J. Lemière, O. Lopez, M. Louvel, M. Mahi, M. Morjean, C. Paulot, A. Péghaire, N. Prot, G. Rudolf, F. Schneibling, J.C. Steckmeyer, B. Tamain, and S. Tomasevic. Phys. Lett. **B 325**, (1994) 317.

[13] S.P. Baldwin, B. Lott, B.M. Szabo, B.M. Quednau, W.U. Schröder, J. Töke, L.G. Sobotka, J. Baretto, R.J. Charity, L. Gallamore, D.G. Sarantites, D.W. Stracener, and R.T. de Souza. Phys. Rev. Lett. **74** , (1995) 1299.

[14] H. Fuchs and K. Möhring. Rep. Prog. Phys. 57, (1994) 231.

[15] J.C. Steckmeyer, G. Bizard, R. Brou, P. Eudes, J.L. Laville, J.B. Natowitz, J.P. Patry, B. Tamain, A. Thiphagne, H. Doubre, A. Péghaire, J. Péter, E. Rosato, J.C. Adloff, A. Kamili, G. Rudolf, F. Scheibling, F. Guibault, C. Lebrun, and F. Hanappe. Nucl. Phys. **A500**, (1989) 372.

[16] B.A. Harmon, J. Pouliot, J.A. Lopez, J. Suro, R. Knop, Y. Chan, D.E. DiGregorio, and R.G. Stokstad. Phys. Lett. **B235**, (1990) 234.

[17] J. Pouliot, G. Auger, P. Bricault, Y. Chan, D. Doré, S. Groult, D. Horn, S. Houde, R. Laforest, R. Roy, and C. St-Pierre. Phys. Lett. **B263**, (1991) 18.

[18] R.J. Charity, J. Barreto, L.G. Sobotka, D.G. Sarantites, D.W. Stracener, A. Chbihi, N.G. Nicolis, R. Aulbe, C. Baktash, J.R. Beene, F. Bertrand, M. Halbert, D.C. Hensley, D.J. Horen, C. Ludemann, M. Thoennessen, and R. Varner. Phys. Rev. C **46** , (1992) 1951.

[19] A. Badalà, R. Barbera, A. Palmeri, and G.S. Pappalardo. Phys. Rev. C **48** , (1993) 633.

[20] P. Désesquelles, A.J. Cole, A. Giorni, A. Lleres, J.B. Viano, B. Chambdon, B. Cheynis, D. Drain, and C. Pastor. Phys. Rev. C **48**, (1993) 1828.

[21] M. Stern, E. Gerlic, R. Billerey, B. Chambon, A. Chevarier, N. Chevarier, B. Cheynis, D. Drain, C. Pastor, C. Vincent-Donnet, A. Giorni, D. Heuer, A. Lleres, J.B. Viano, and P.L. Gonthier. Nucl. Phys. **A559**, (1993) 401.

[22] R. Laforest, D. Doré, S. Houde, J. Pouliot, R. Roy, C. St. Pierre, G. Auger, P. Bricault, S. Groult, E. Plagnol, and D. Horn. Nucl. Phys. **A568**, (1994) 350.

[23] D. Doré, L. Beaulieu, R. Laforest, J.L. Laville, O. Lopez, J. Pouliot, R. Régimbart, R. Roy, J.C. Steckmeyer, and C. St-Pierre. Phys. Lett. **B 323**, (1994) 103.

[24] L. Beaulieu, R. Laforest, J. Pouliot, R. Roy, C. St-Pierre, G.C. Ball, E. Hagberg, D. Horn, and R.B. Walker. Nucl. Phys. **A580**, (1994) 81.

[25] J. Pouliot, L.Beaulieu, B. Djerroud, D. Doré, R. Laforest, R. Roy, C. St-Pierre, and J. A. Lòpez. Phys. Rev. C **48**, (1993) 2514.

[26] M. Samri, L. Beaulieu, B. Djerroud, D. Doré, P. Gendron, E. Jalbert, R. Laforest, Y. Larochelle, J.Pouliot, R. Roy, C. St-Pierre, G.C. Ball, A. Galindo-Uribarri, E. Hagberg, and D. Horn. Nucl. Phys. **A583**, (1995) 427c .

[27] L.G. Moretto, D.N. Delis, and G.J. Wozniak. Phys. Rev. Lett. **71**, (1993) 3935.

[28] R.J. Charity, L.G. Sobotka, G. Van Buren, F.A. Tibbals, J. Barreto, D.R. Bowman, M. Chartier, J. Dinius, D. Fox, C.K. Gelbke, D.O. Handzy, W.C. Hsi, P.F. Hua, A.S. Kirov, M.A. Lisa, W.C. Lynch, G.F. Peaslee, L. Phair, D.G. Sarantites, C. Schwartz, R.T. de Souza, M.B. Tsang, and C. Williams. Phys. Lett. **B323**, (1994) 113.

[29] M. Samri, L. Beaulieu, B. Djerroud, D. Doré, P. Gendron, E. Jalbert, R. Laforest, Y. Larochelle, J.Pouliot, R. Roy, C. St-Pierre, G.C. Ball, A. Galindo-Uribarri, E. Hagberg, and D. Horn. to be published.

[30] C. Pruneau, D. Horn, M.G. Steer, R.B. Walker, T. Whan, C. Rioux, R. Roy, C. St-Pierre, T.E. Drake, and A. Galindo-Uribarri. Nucl. Inst. and Meth. **A297**, (1990)

404.

[31] Y. Larochelle, L. Beaulieu, B. Djerroud, D. Doré, P. Gendron, E. Jalbert, R. Laforest., J. Pouliot, R. Roy, M. Samri, and C. St-Pierre. Nucl. Instr. and Meth. in Phys. Res. **A348**, (1994)167.

[32] W.W. Wilke, J.R. Birkelund, H.J. Wollersheim, A.D. Hoover, J.R. Huizenga, W.U. Schröder, and L.E. Tubbs. Atom. and Nucl. Data. Tab.**25**, (1980) 389.

[33] A. Lleres, A. Giorni, H. Elhage, M.E. Brandan, A. J. Cole, P. Désesquelles, D. Heuer, A. MenchacaRocha, J. B. Viano, F. Benrachi, B. Chambon, B. Cheynis, D. Drain, and C. Pastor. Phys. Rev. C **48**, (1993) 2753.

[34] L. Beaulieu, M. Samri, G. Anctil, B. Djerroud, D.R. Bowman, G.C. Ball, D. Doré, A. Galindo-Uribarri, P. Gendron, D. Guinet, E. Hagberg, D. Horn, E. Jalbert, R. Laforest, Y. Larochelle, P. Lautesse, R. Roy and C. St-Pierre. to be published

[35] J. Pouliot, Y. Chan, A. Dacal, A. Harmon, R. Knop, M.E. Ortiz, E. Plagnol, and R.G. Stokstad. Nucl. Instr. and Meth. in Phys. Res. **A270**, (1988)69.

[36] H. Morinaga. Phys. Rev. **101**, (1956) 254.

[37] A.H. Wuosmaa, R.R. Betts, B.B. Back, M. Freer, B.G. Glagola, Th. Happ, D.J. Henderson, P. Wilt and I.G. Bearden. Phys. Rev. Lett. **68**, (1992) 1295.

[38] R.J. Charity, M.A. McMahan, G.J. Wozniak, R.J. McDonald, L.G. Moretto, D.G. Sarantites, L.G. Sobotka, G. Guerino, A. Pantaleo, L. Fiore, A. Gobbi, and K.D. Hildenbrand. Nucl. Phys. **A483**, (1988) 371.

[39] R. Schmidt and H.O. Lutz. Phys. Rev. A **45**, (1992) 7981.

[40] C.A. Ogilvie, D.A. Cebra, J. Clayton, P. Danielewicz, S. Howden, J. Karn, A. Nadasen, A. Vander Molen, G.D. Westfall, W.K. Wilson, and J.S. Winfield. Phys. Rev. **C 40**, (1989) 2592.

[41] H. Ströbele, R. Brockmann, J.W. Harris, F. Riess, A. Sandoval, R. Stock, K.L. Wolf, H.G. Pugh, L.S. Schroeder, R.E. Renfordt, K. Tittel, and M. Maier. Phys. Rev. C **27**, (1983) 1349.

[42] C.H. Dasso and G. Pollarolo. Comp. Phys. Comm. **50**, (1988) 341.

[43] O. Lopez. PhD thesis, Université de Caen, (1993) (unpublished).

[44] Y. Larochelle, G.C. Ball, L. Beaulieu, B. Djerroud, D. Doré, A. Galindo-Uribarri, P. Gendron, E. Hagberg, D. Horn, E. Jalbert, R. Laforest, J. Pouliot, R. Roy, M. Samri, and C. St-Pierre. Phys. Lett. **B 352**, (1995) 8.

[45] D. Horn, G.C. Ball, D.R. Bowmann, A. Galindo-Uribarri, E. Hagberg, R. Laforest, J. Pouliot, and R.B. Walker. Proceedings of the Workshop on Heavy-Ion Fusion, Padua, Italy, 1994 May 25-27, ed. A.M. Stefanini, G. Nebbia, S. Lunardi, G.Montagnoli and A. Vitturi, World Scientific.

[46] D. Horn, G.C. Ball, D.R. Bowmann, A. Galindo-Uribarri, E. Hagberg, R. Laforest, J. Pouliot, and R.B. Walker. Proceedings of the Workshop on Nuclear Dynamics, Key West, USA, 1995 Feb 11-17, to be published.

[47] H. Morgenstern, W. Bohne, W. Galster, K. Grabisch, and A. Kyanowski. Phys. Rev. Lett. **52**, (1984) 1104.

[48] A. Malki, J.P. Coffin, G. Guillaume, F. Jundt, K. Krishan, F. Rami, P. Wagner, P. Fintz, M. Zahar, M. Gonin, B. Heusch, M. Ohta, B. Rastegar, D. Rebreyend, F. Merchez, J. Mistretta, and S. Kox. Z. Phys. A **339**, (1991) 283.

[49] J.P. Wieleczko, E. Plagnol, and P. Ecomard. Proceedings of the 2^{nd} TAPS Workshop 1994, ed. by Diaz, Martinez and Schutz, Guardemar , World Scientific, p.145 .

[50] D.R. Bowman, G.F. Peaslee, R.T. de Souza, N. Carlin, C.K. Gelbke, W.G. Gong, Y.D. Kim, M.A. Lisa, W.G. Lynch, L. Phair, M.B. Tsang, C. Williams, N. Colonna, K.

Hanold, M.A. McMahan, G.J. Wozniak, L.G. Moretto and W.A. Friedman. Phys. Rev. Lett. **67**, (1991) 1527.

TABLES

TABLE I. Detection efficiency for Z=1-12 ions for ^{24}Mg+^{12}C reaction at 25A and 35A MeV and for ^{35}Cl+^{197}Au reaction at 43A MeV.

TABLE II. Calculated cross sections and Q_0 value, with mass $\equiv$ 2Z (except for Z=1 particles which are all considered as protons), for a subset of 25 exit channels for the ^{24}Mg+^{12}C reaction at 25A and 35A MeV and for the ^{35}Cl+^{197}Au reaction at 43A MeV with EBC.

TABLE III. Input parameters for GEMINI simulations.

TABLE IV. Mean values of R_A, and R_K and their variance for data and simulations. Input parameters for the simulations are given in Table III.

FIGURES

FIG. 1. Experimental set-up, the CRL-Laval Array. See text for description.

FIG. 2. Reconstructed center-of-mass velocity for exit channels with ΣZ=12 and ΣZ=18 from the ^{24}Mg+^{12}C reaction at 25A MeV (top) and 35A MeV (middle) and reconstructed QP velocity with ΣZ=18 for ^{35}Cl+^{197}Au at 43A MeV(bottom). The arrows indicate beam velocity and CM velocity for the complete system of target and projectile.

FIG. 3. Charge distribution for exit channels with total charge detected (ΣZ = 18) in the ^{24}Mg+^{12}C reaction at 25A MeV (top left) and 35A MeV (bottom left) and ^{35}Cl+^{197}Au at 43A MeV with ΣZ(QP) = 18 with EBC (top right) and without EBC (bottom right).

FIG. 4. Cross sections for charged particles, plotted as a function of laboratory velocity and element number, for exit channels with total charge detected in the ^{24}Mg+^{12}C reaction at 25A MeV (top left) and 35A MeV (bottom left) and ^{35}Cl+^{197}Au at 43A MeV with ΣZ=18 with EBC (top right) and without EBC (bottom right). The dots represent the energy thresholds of the detectors. Arrows show beam and CM velocity for ^{24}Mg+^{12}C data at 25A MeV (0.23c and 0.15c respectively) and 35A MeV (0.27c and 0.18c) and beam velocity for ^{35}Cl+^{197}Au data at 43A MeV.

FIG. 5. Charged-particle multiplicity distribution for exit channels with total charge detected in the ^{24}Mg+^{12}C reaction at 25A MeV (top left) and 35A MeV (bottom left) and ^{35}Cl+^{197}Au at 43A MeV with ΣZ(QP) = 18 with EBC (top right) and without EBC (bottom right).

FIG. 6. Cross sections for $\Sigma Z = 18$ events, as a function of excitation energy, corrected for undetected neutrons in the ^{24}Mg+^{12}C reaction at 25A MeV (top left, $< E^* >= 190$ MeV) and 35A MeV (bottom left, $< E^* >= 248$ MeV) and ^{35}Cl+^{197}Au at 43A MeV with ΣZ(QP) = 18 with EBC (top right, $< E^* >= 224$ MeV) and without EBC (bottom right, $< E^* >= 192$ MeV). Arrows show CM energy for central reactions (200 MeV in ^{24}Mg+^{12}C at 25A MeV and 280 MeV in ^{24}Mg+^{12}C at 35A MeV).

FIG. 7. Cross sections (in arbitrary units) for simulated ΣZ(detected)=18 events, as a function of excitation energy. The events are generated with the code GEMINI, filtered by the experimental acceptance, corrected for undetected neutrons, and reconstructed in the same way as the experimental events. Simulations of ^{36}Ar* with E^*=200 MeV in the central scenario for ^{24}Mg+^{12}C at 25A MeV are plotted in the top left (mean $< E^* >= 198$ MeV); those for the peripheral scenario for ^{35}Cl+^{197}Au at 43A MeV with EBC are plotted in the top right (mean $< E^* >= 217$ MeV). Simulations of ^{36}Ar* with E*=280 MeV in the central scenario for ^{24}Mg+^{12}C at 35A MeV are at the bottom left (mean $< E^* >= 261$ MeV), and those the peripheral scenario for ^{35}Cl+^{197}Au at 43A MeV with E*=280 MeV and with EBC are at the bottom right (mean $< E^* >= 261$ MeV). Arrows show the center-of-mass energies for the ^{24}Mg+^{12}C reactions at 25A MeV and 35A MeV.

FIG. 8. Anisotropy ratio distributions for events with excitation energy between 170 and 230 MeV, for central data at 25A MeV (full dots) and the corresponding filtered GEMINI simulation (full line), peripheral data at 43A MeV with EBC (empty dots) and corresponding simulation (dashed line). The yields of the distributions are in arbitrary units. The errors bars represent statistical errors.

FIG. 9. Same as Fig. 8 but for data and simulations corresponding to ^{24}Mg+^{12}C at 35A MeV and excitation energy between 250 and 310 MeV.

FIG. 10. Centroids of the anisotropy ratios, R_A as defined in eq. (3), versus charged-particle multiplicity for incompletely detected events (ΣZ=15,16,17) at 25A MeV (top left) and 35A MeV (bottom left). Completely detected experimental events (ΣZ=18) and the corresponding filtered simulations are shown for 25A MeV (top right) and 35A MeV (bottom right). Filled circles represent experimental data, open squares complete fusion simulations with GEMINI, and open triangles dissipative-binary collision simulations with TORINO and GEMINI. Error bars are the root-mean square divided by the square-root of the number of counts of the anisotropy distribution for a given multiplicity. Distributions with less than 25 counts were rejected. The horizontal lines represent R_A centroids averaged over all multiplicities for unfiltered simulations with the same codes, for complete fusion (full lines) and dissipative binary collisions (dashed lines).

FIG. 11. Anisotropy ratio (R_A) versus kinetic energy fraction ratio (R_K) for events with excitation energy between 170 and 230 MeV, for central ^{24}Mg+^{12}C data at 25A MeV (top left), the corresponding filtered GEMINI simulation (middle left), peripheral ^{35}Cl+^{197}Au data at 43A MeV with EBC (top right), the corresponding simulation (middle right) and the unfiltered simulation (bottom left). Arrows show the average R_K for each distribution.

FIG. 12. Same as Figure 11 but for events with excitation energy between 250 and 310 MeV and central ^{24}Mg+^{12}C data at 35A MeV (top left).

FIG. 13. Differences between data and simulations for mean values of R_A and R_K distributions. The axes are in χ^2 units; see text for details.

FIG. 14. Parallel-versus-perpendicular velocity plot of pre-equilibrium proton emission in incomplete fusion reactions of ^{24}Mg + ^{12}C at 35A MeV, simulated with the code GENEVE. Lines represent the geometric and energetic thresholds of the array of detectors for protons. Arrows show projectile (0.27c), CM (0.18c) and target (0.0c) velocities.

FIG. 15. Centroids of the anisotropy ratios, R_A as defined in eq. (3), versus charged-particle multiplicity for ^{24}Mg + ^{12}C data at 35A MeV with ΣZ=18 (full circles) and filtered GENEVE simulations of incomplete fusion (open squares), PLF-TLF events (open triangles), and their total (stars). The unfiltered incomplete fusion anisotropy generated by GENEVE, averaged over all charged-particle multiplicities, is shown as the full line. Error bars represent the root-mean square of the anisotropy ratio distributions divided by the square-root of the number of counts of for a given multiplicity.

FIG. 16. Average IMF multiplicity versus excitation energy for ^{24}Mg + ^{12}C data (full circles) at 25A MeV (left) and 35A MeV (right) and the corresponding filtered GEMINI simulations (full lines), and for peripheral ^{35}Cl+^{197}Au data at 43A MeV with EBC (open circles) and the corresponding the GEMINI simulations (dashed lines). Arrows show the center-of-mass energies for the ^{24}Mg + ^{12}C reactions. Error bars are the root-mean square of the IMF multiplicity distributions for each bin of excitation energy, divided by the square-root of the number of counts, and are displayed only when larger than the symbols.

FIG. 17. Yields for exit channels with a heavy residue (dots), dissipative evaporation and/or fission (squares), multifragmentation (triangles) and vaporization (stars), for events with excitation energy between 170 and 230 MeV, for central ^{24}Mg + ^{12}C data at 25A MeV (top left) and the corresponding filtered GEMINI simulation (middle left), peripheral ^{35}Cl+^{197}Au data at 43A MeV with EBC (top right) and corresponding filtered simulation (middle right) and unfiltered simulation (bottom left). Error bars represent statistic errors.

FIG. 18. Same as Figure 17 but for events with excitation energy between 250 and 310 MeV and central ^{24}Mg + ^{12}C data at 35A MeV (top left).

Charge	Detection Efficiency $\varepsilon(Z)$ (ΣZ=18) ^{24}Mg+^{12}C at 25A and 35A MeV	Detection efficiency $\varepsilon(Z)$ (ΣZ=18) ^{35}Cl+^{197}Au at 43A MeV
1	0.74	0.72
2	0.69	0.76
3	0.78 (25A MeV)	0.74
3	0.44 (35A MeV)	0.74
4	0.48	0.42
5	0.64	0.62
6	0.63	0.65
7	0.57	0.63
8	0.45	0.55
9	0.38	0.49
10	0.26	0.39
11	0.20	0.30
12	0.28	0.37

TABLE I. Y.Larochelle et al.

Exit channel	Q_0 (MeV)	σ (mb)	σ (mb)	σ (mb)
	^{36}Ar	Mg+C(25)	Mg+C(35)	Cl+Au(43)
Ne C H H	-37.77	0.0013	0.00061	0.80
Mg He He H H	-35.73	0.0038	0.020	0.18
N C He He H	-45.23	0.0022	0.0013	5.69
F B He H H	-60.16	0.00043	0.0018	3.14
Mg He H H H H	-47.88	0.00069	0.034	0.024
F He He He He H	-48.09	0.18	0.24	4.38
C B He He He H	-56.85	0.11	0.066	9.00
O Li Li He H H	-70.67	0.0085	0.0067	1.49
O He He He He H H	-49.77	0.48	1.22	15.41
C Be He He He H H	-57.02	0.39	0.53	19.32
F He He He H H H	-60.25	0.082	0.58	8.55
B Li He He He He He	-68.50	0.18	0.043	1.22
N Li He He He H H	-69.03	0.26	0.28	11.51
Be Li Li He He He He	-73.05	0.11	0.029	0.71
B B Li He H H H	-92.71	0.0039	0.0032	1.72
C He He He He He H H	-56.93	0.98	1.96	17.38
O He He He H H H H	-61.93	0.085	1.15	14.18
C Li Li He H H H H	-89.99	0.0045	0.024	1.88
Li Li Li Li He He H H	-106.00	0.0029	0.0056	0.16
He He He He He He He He He	-52.06	0.17	0.18	0.26
C He He He He H H H H	-69.09	0.29	2.12	20.16
Be Li He He He He H H H	-80.83	0.30	1.21	14.47
Li He He He He He He H H H	-80.74	0.45	2.63	7.87
He He He He He He He H H H H	-76.36	0.20	2.20	5.00

He He He He He He H H H H H H	-88.52	0.014	0.40	2.53

TABLE II. Y.Larochelle et al.

Case	Reaction	E^*_{Ar} [MeV]	V_{Ar} [c]	θ_{Ar} [degree]	Angular Momentum [$\hbar$]
A	^{24}Mg+^{12}C at 25A MeV central	200	0.15	0^o	25
B	^{35}Cl+^{197}Au at 43A MeV peripheral	200	0.23	6^o	25
C	^{24}Mg+^{12}C at 35A MeV central	280	0.18	0^o	25
D	^{35}Cl+^{197}Au at 43A MeV peripheral	280	0.23	6^o	25

TABLE III. Y.Larochelle et al.

Reaction	E* [MeV]	$< R_A >$	Variance $[\sigma^2]$	$< R_K >$	Variance $[\sigma^2]$
Experiments					
^{24}Mg+^{12}C at 25A MeV	170-230	1.1	0.1	0.57	0.003
^{35}Cl+^{197}Au at 43A MeV	170-230	1.2	0.2	0.58	0.004
^{24}Mg+^{12}C at 35A MeV	250-310	0.9	0.1	0.63	0.003
^{35}Cl+^{197}Au at 43A MeV	250-310	1.1	0.2	0.60	0.003
Simulations with GEMINI					
^{36}Ar* E^*_{Ar}=200 MeV central	170-230	1.3	0.2	0.50	0.003
^{36}Ar* E^*_{Ar}=200 MeV peripheral	170-230	1.2	0.2	0.54	0.003
^{36}Ar* E^*_{Ar}=280 MeV central	250-310	1.3	0.2	0.55	0.002
^{36}Ar* E^*_{Ar}=280 MeV peripheral	250-310	1.2	0.2	0.55	0.002

TABLE IV. Y.Larochelle et al.

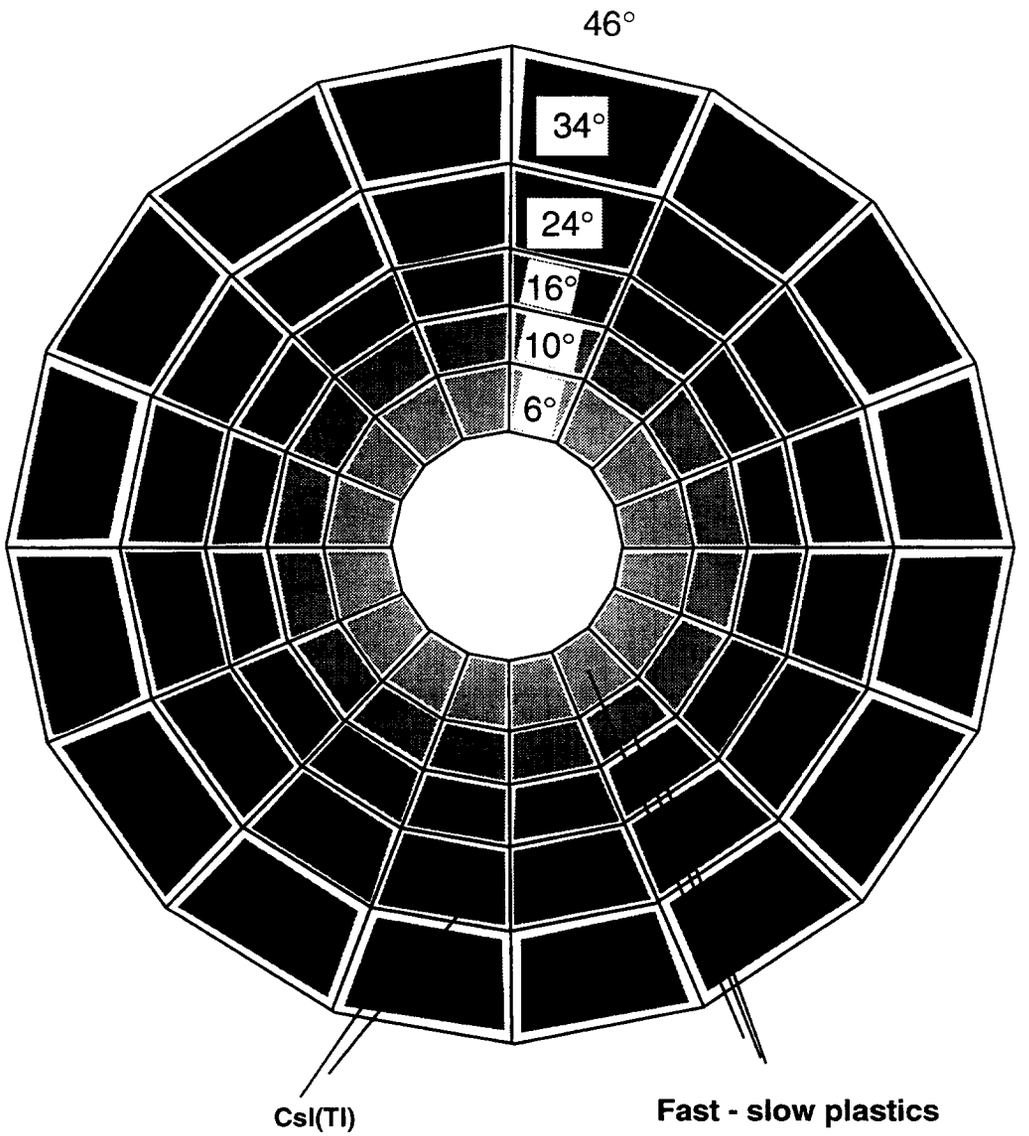

FIG. 1. Y.Larochelle et al.

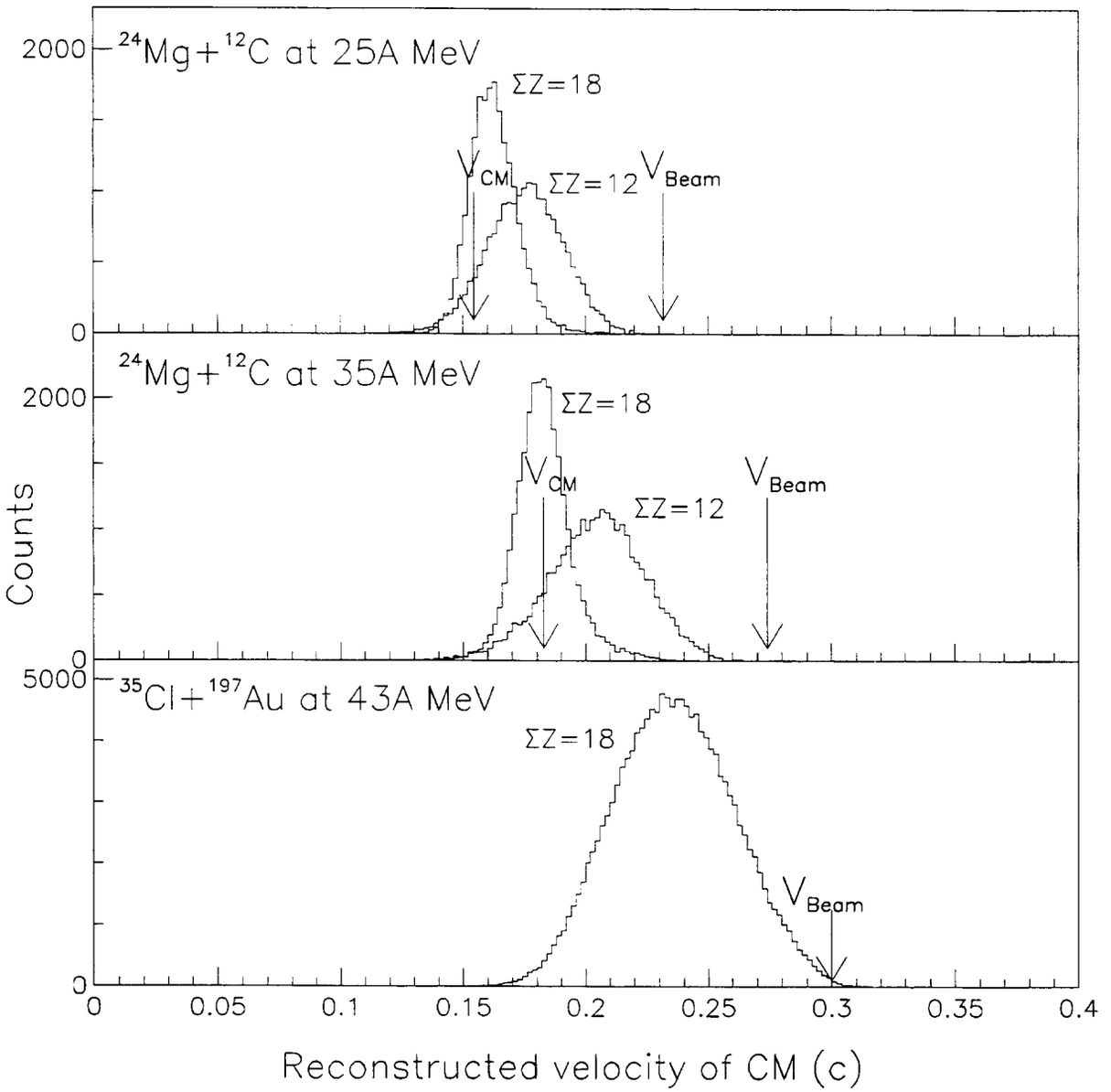

FIG. 2. Y.Larochelle et al.

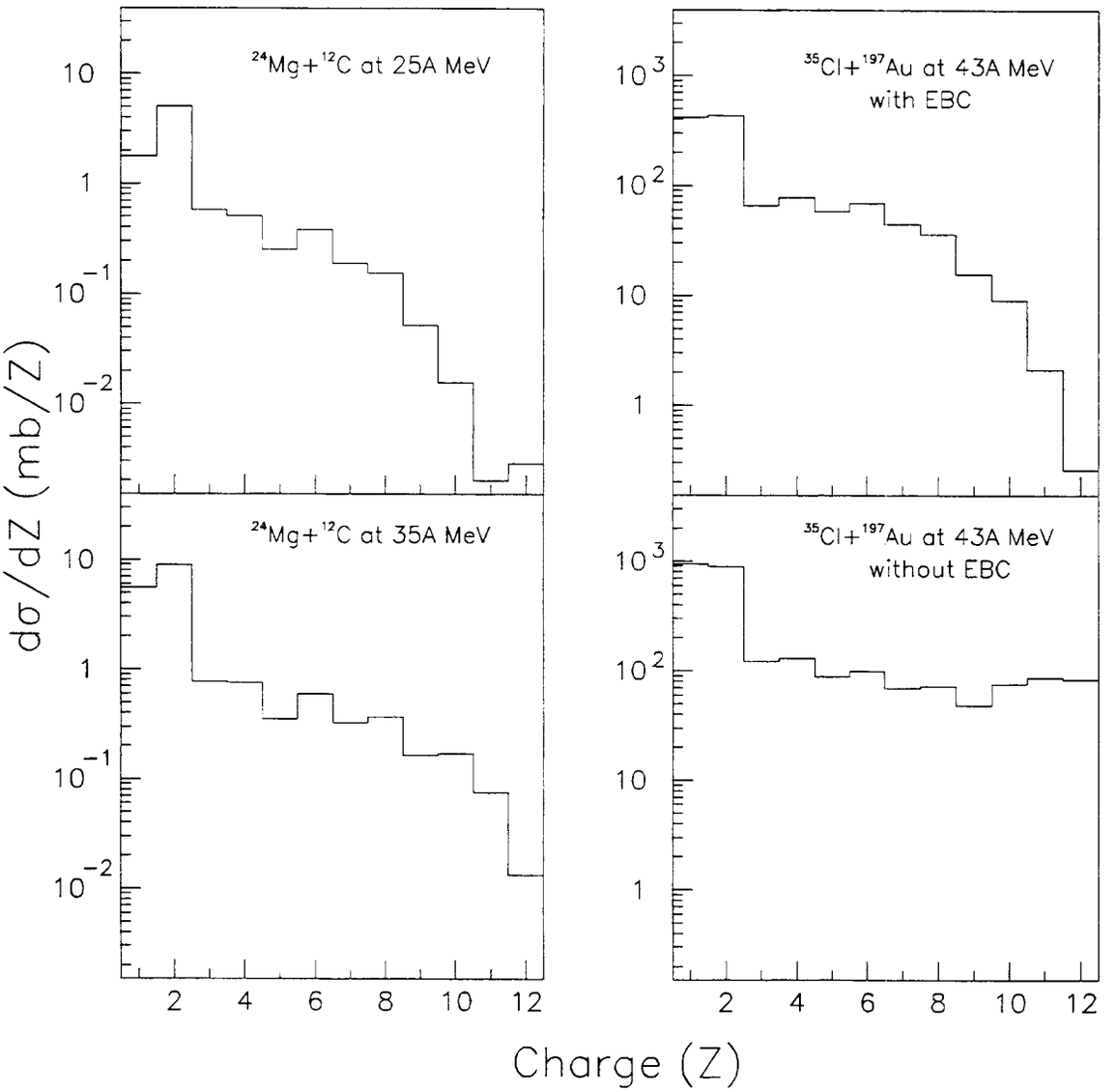

FIG. 3. Y.Larochelle et al.

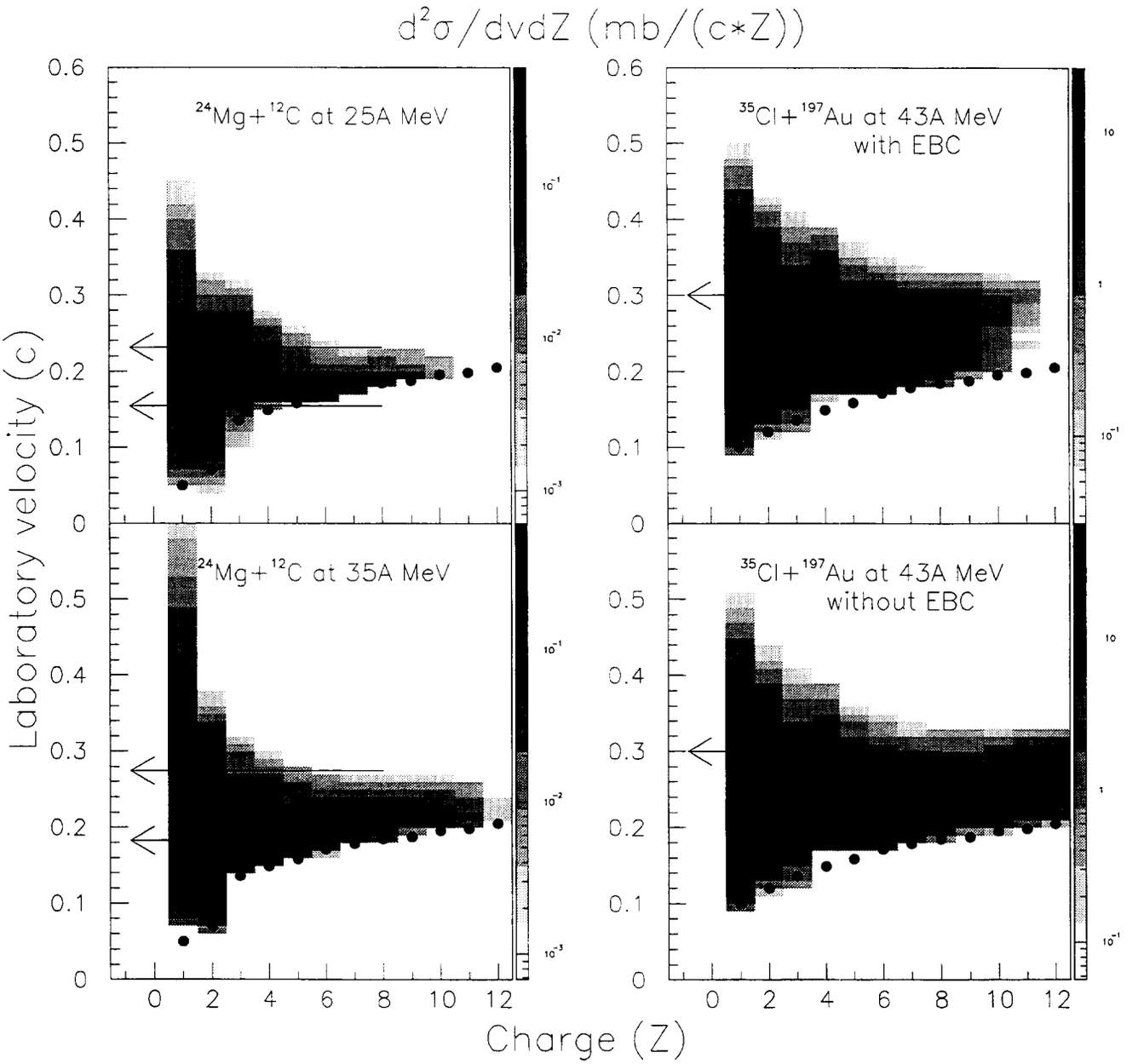

FIG. 4. Y.Larochelle et al.

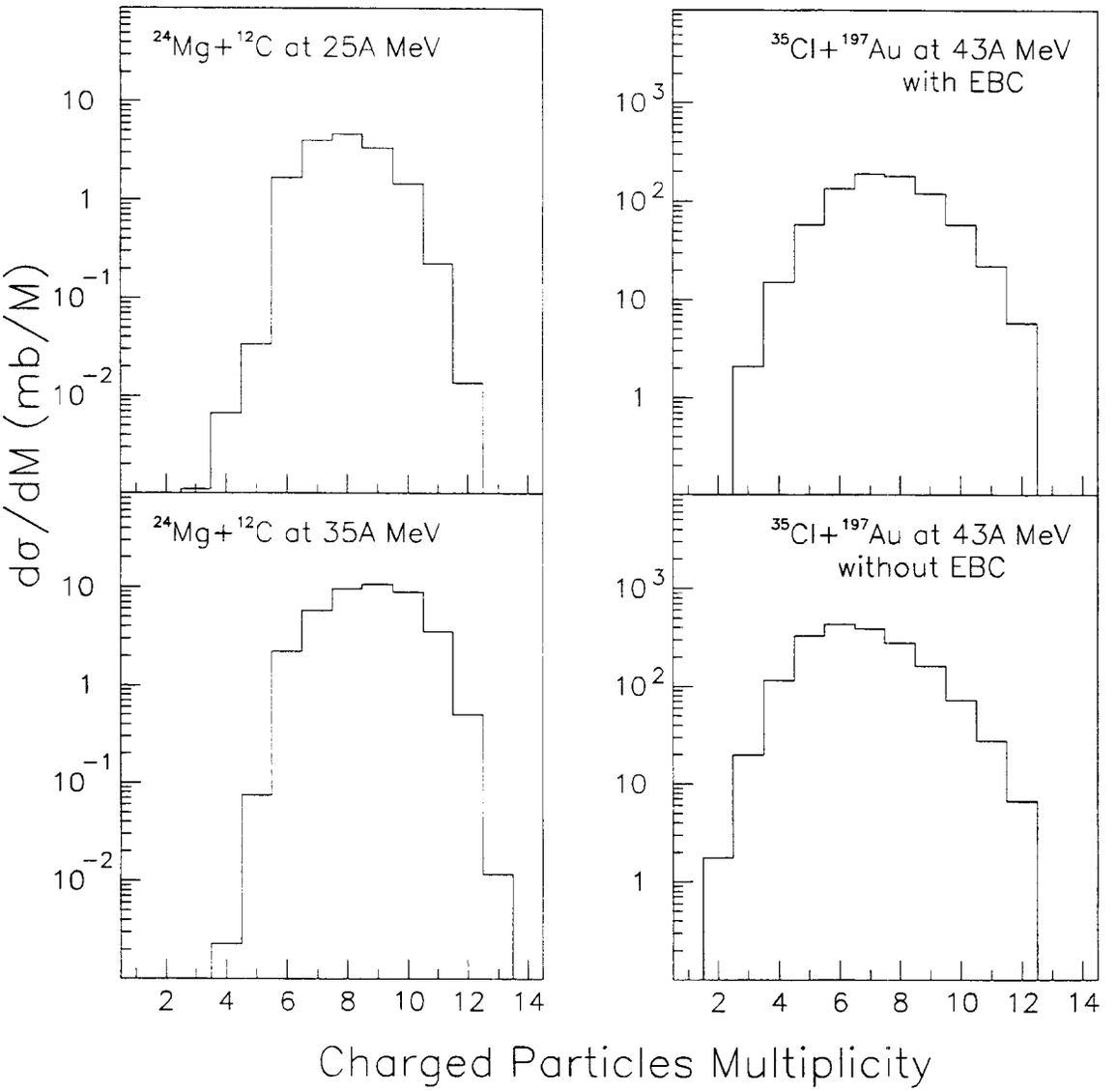

FIG. 5. Y.Larochelle et al.

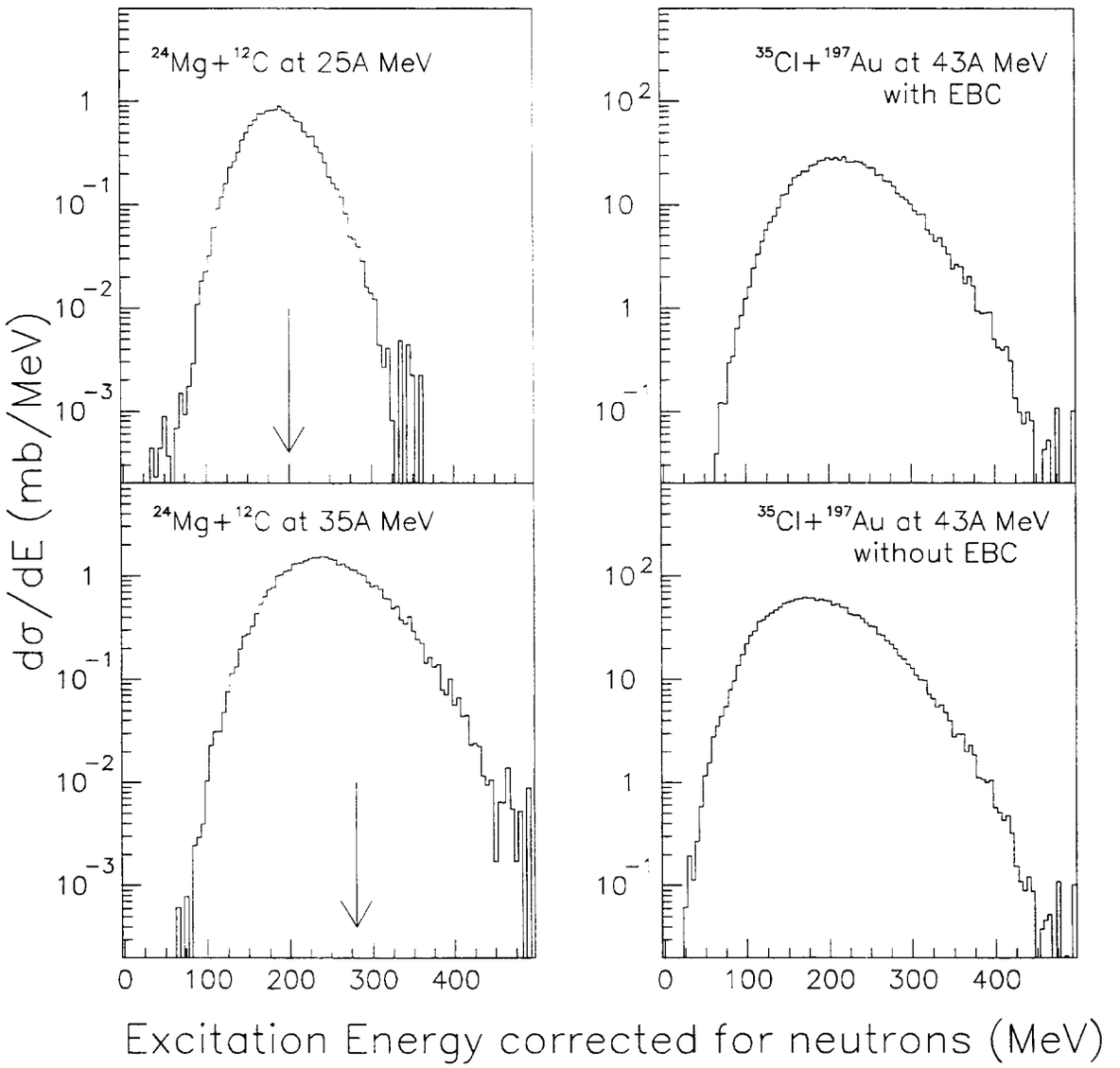

FIG. 6. Y.Larochelle et al.

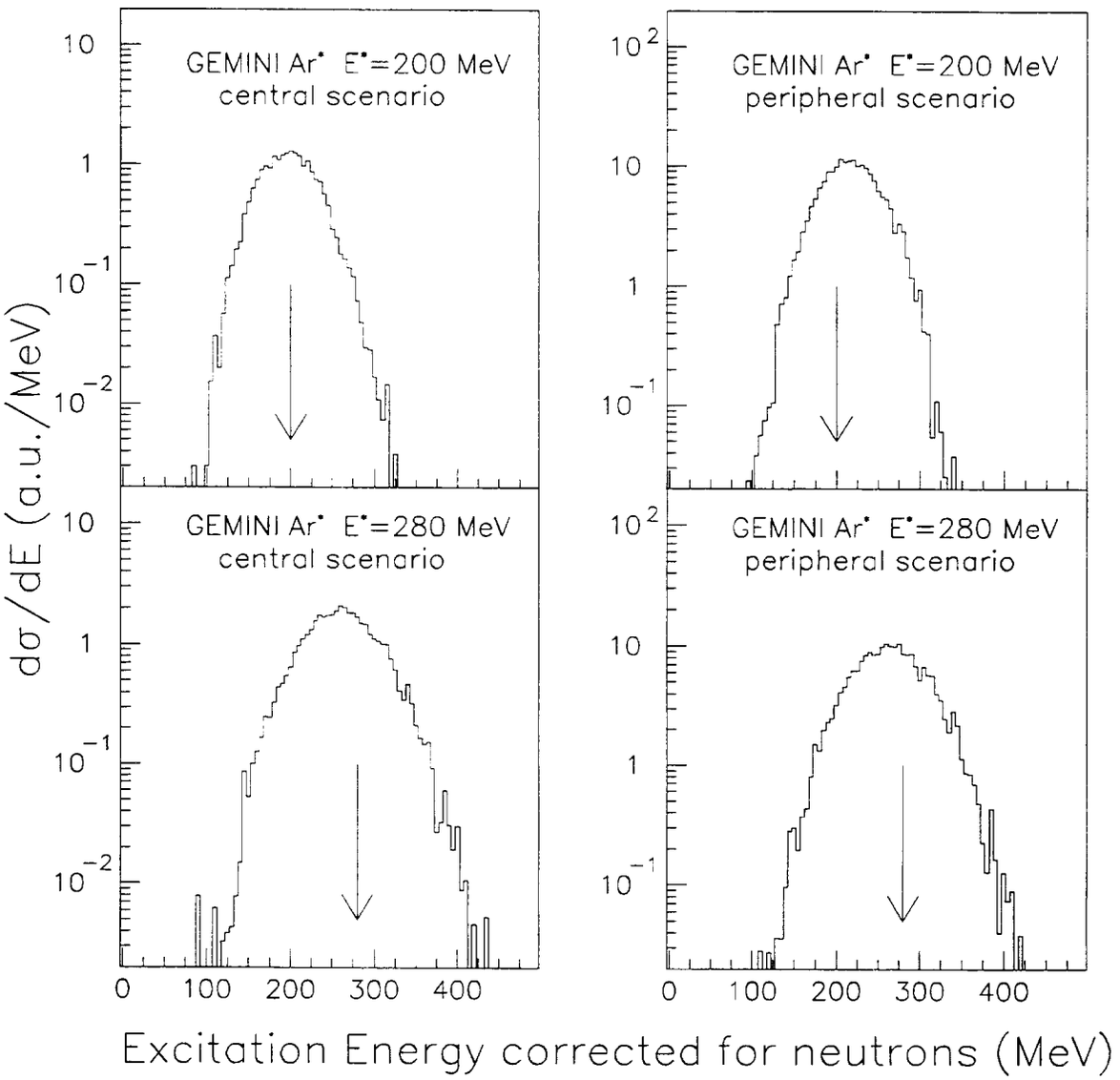

FIG. 7. Y.Larochelle et al.

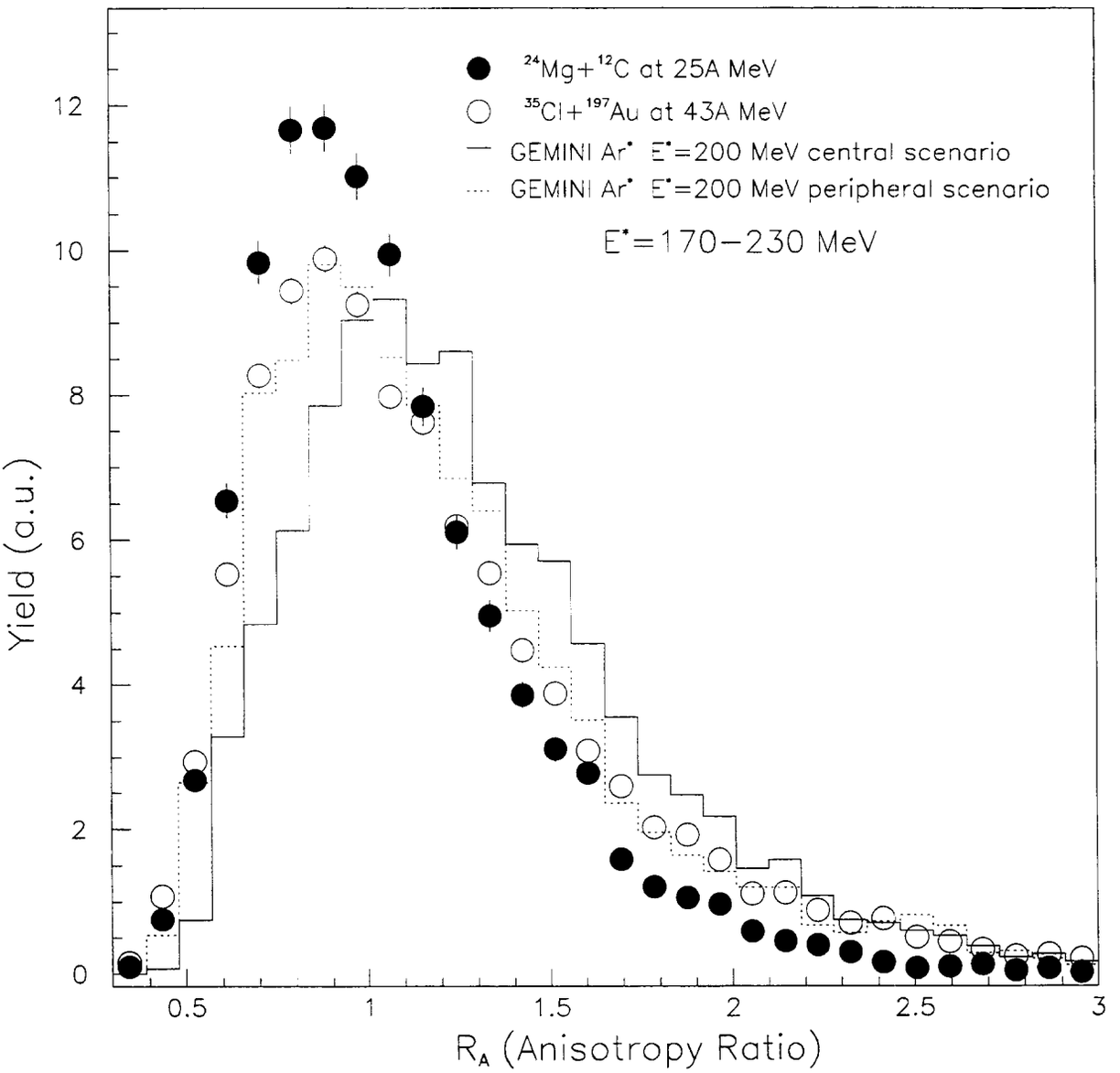

FIG. 8. Y.Larochelle et al.

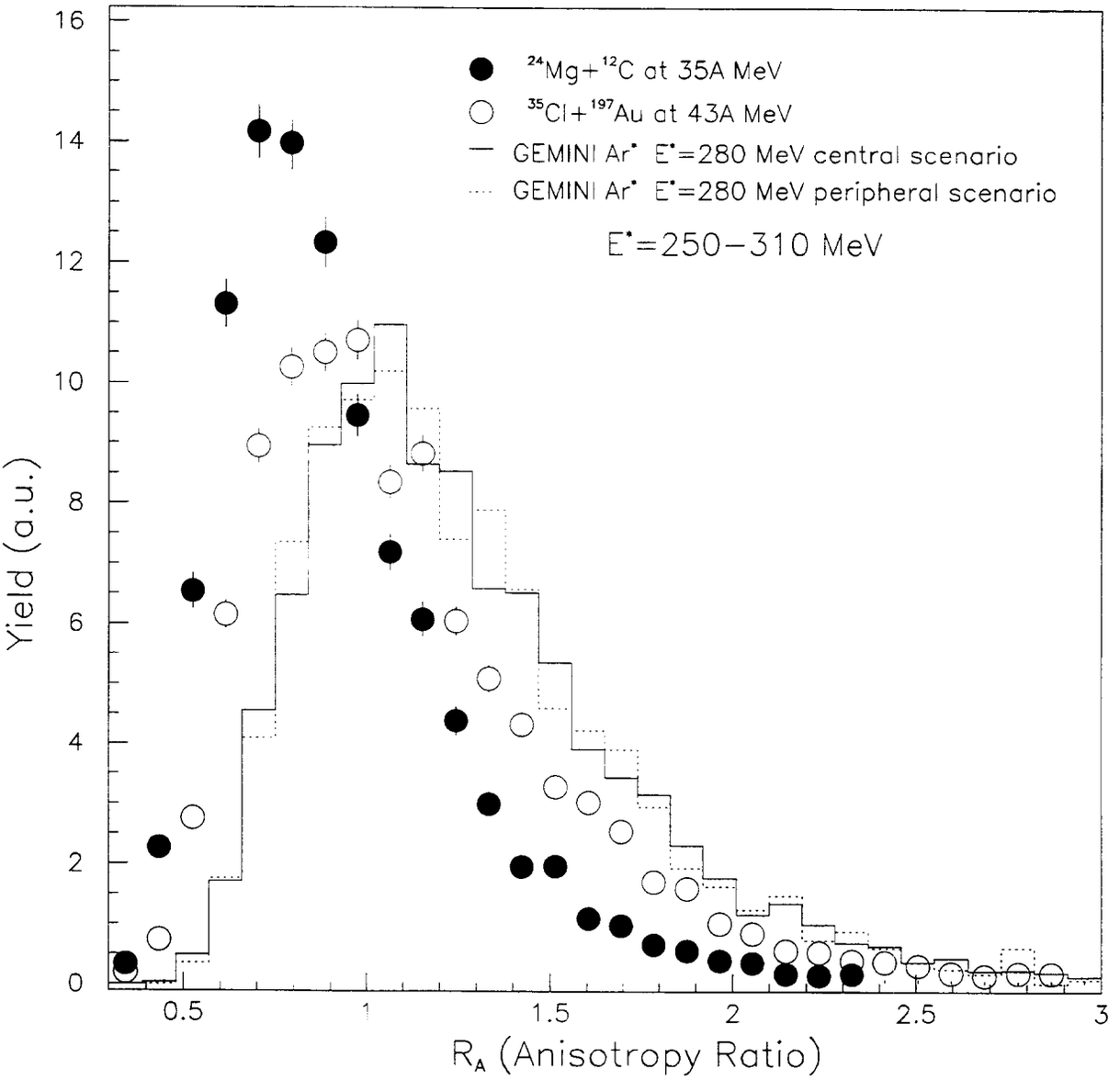

FIG. 9. Y.Larochelle et al.

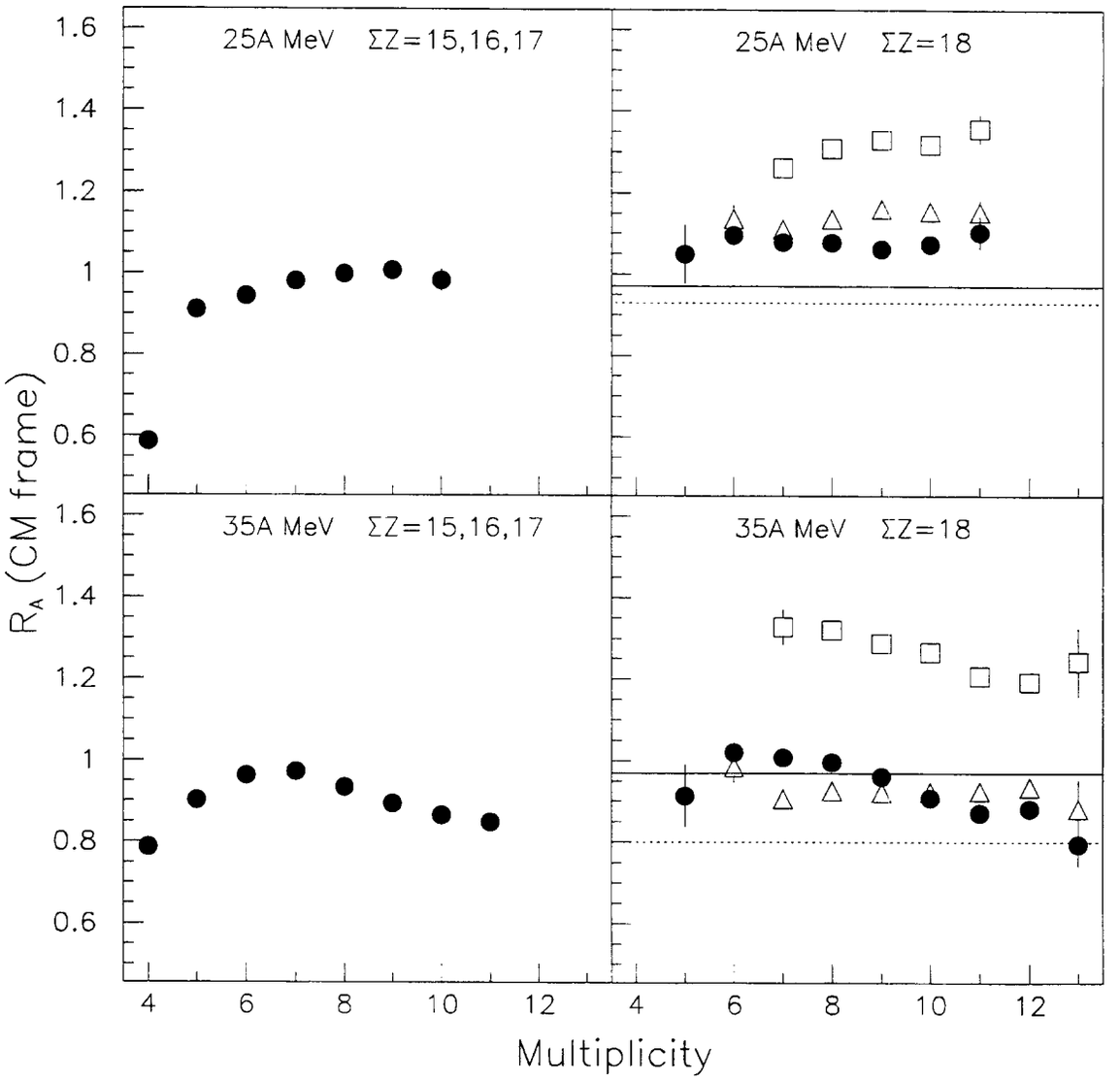

FIG. 10. Y.Larochelle et al.

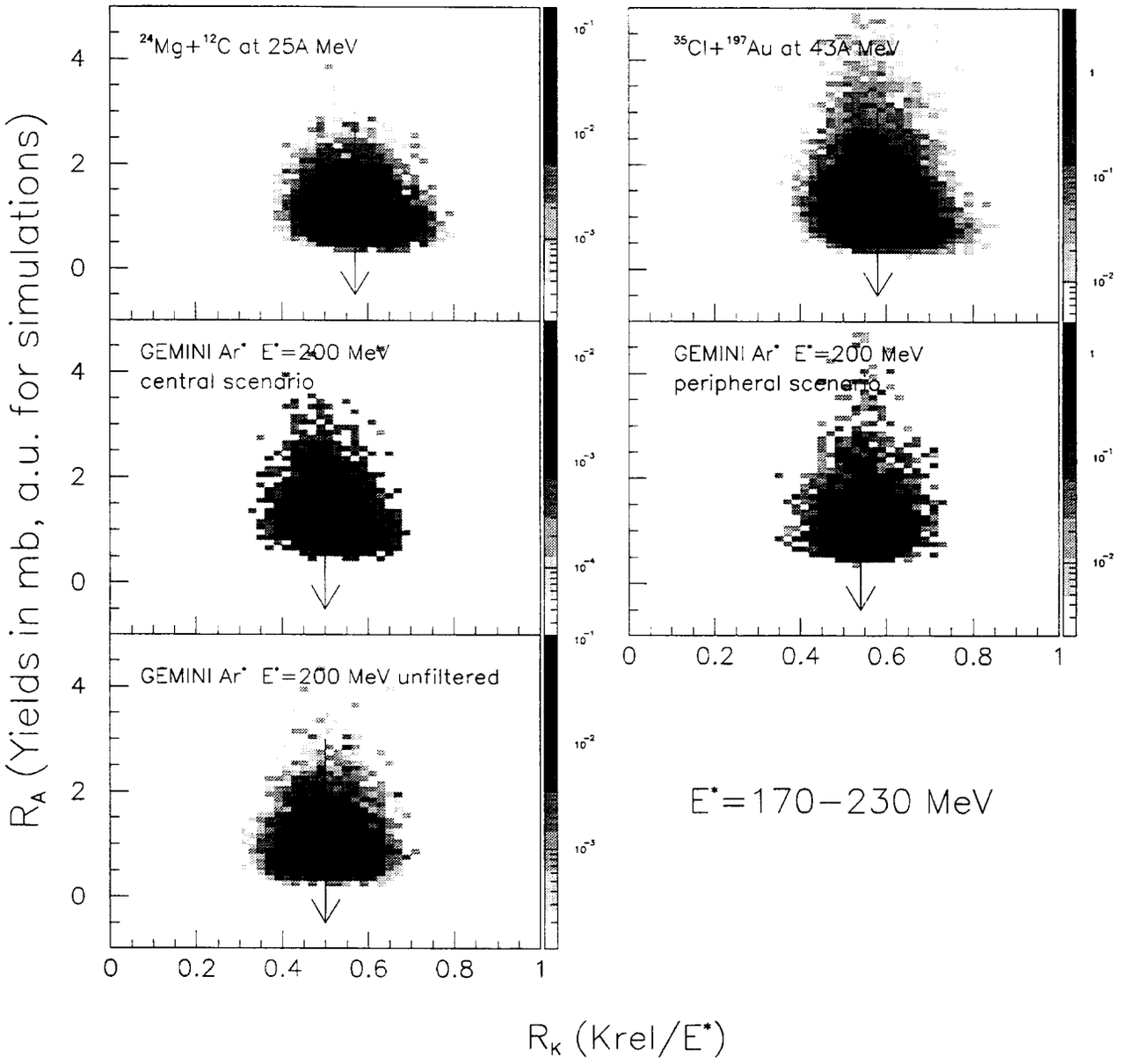

FIG. 11. Y.Larochelle et al.

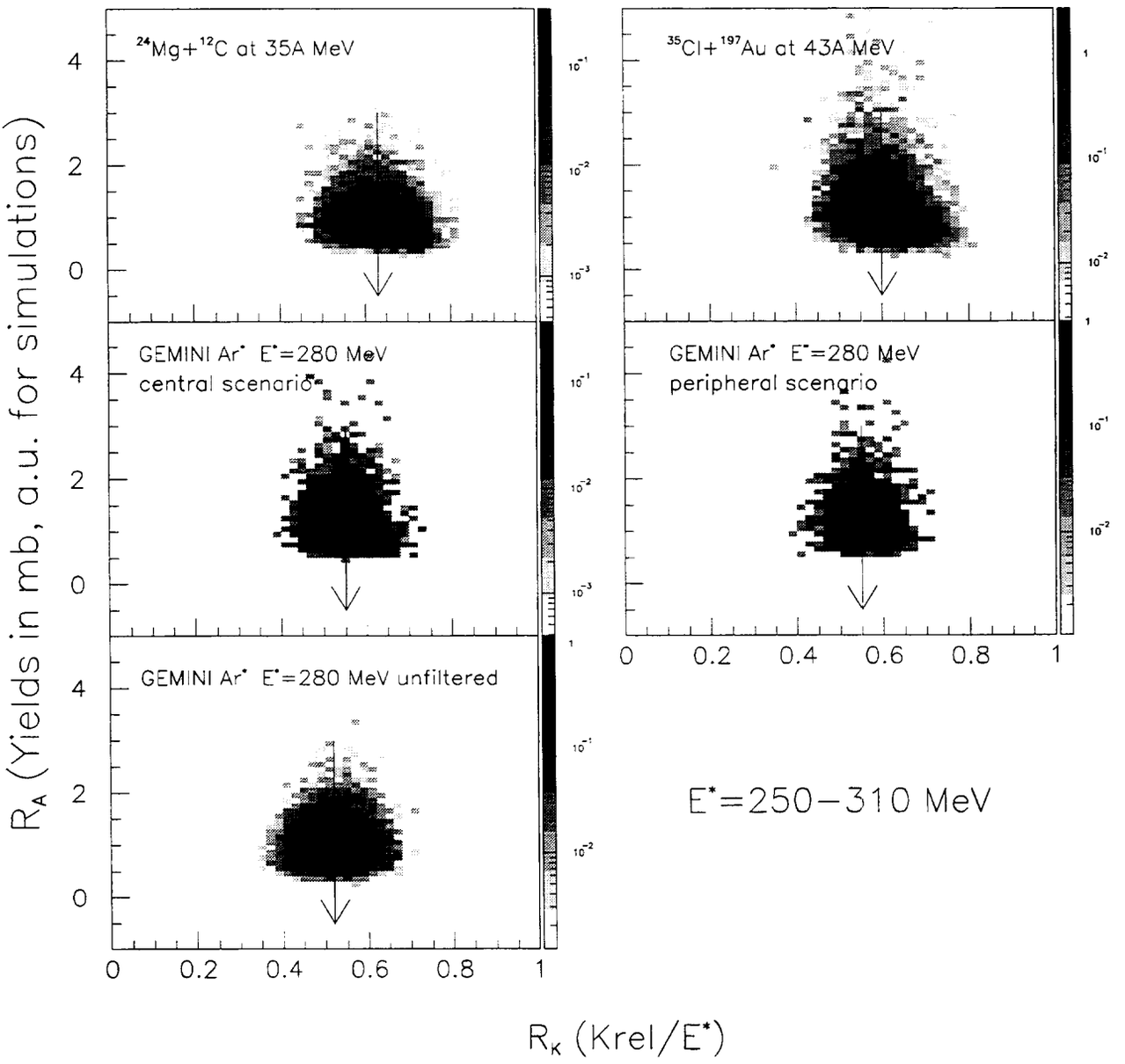

FIG. 12. Y.Larochelle et al.

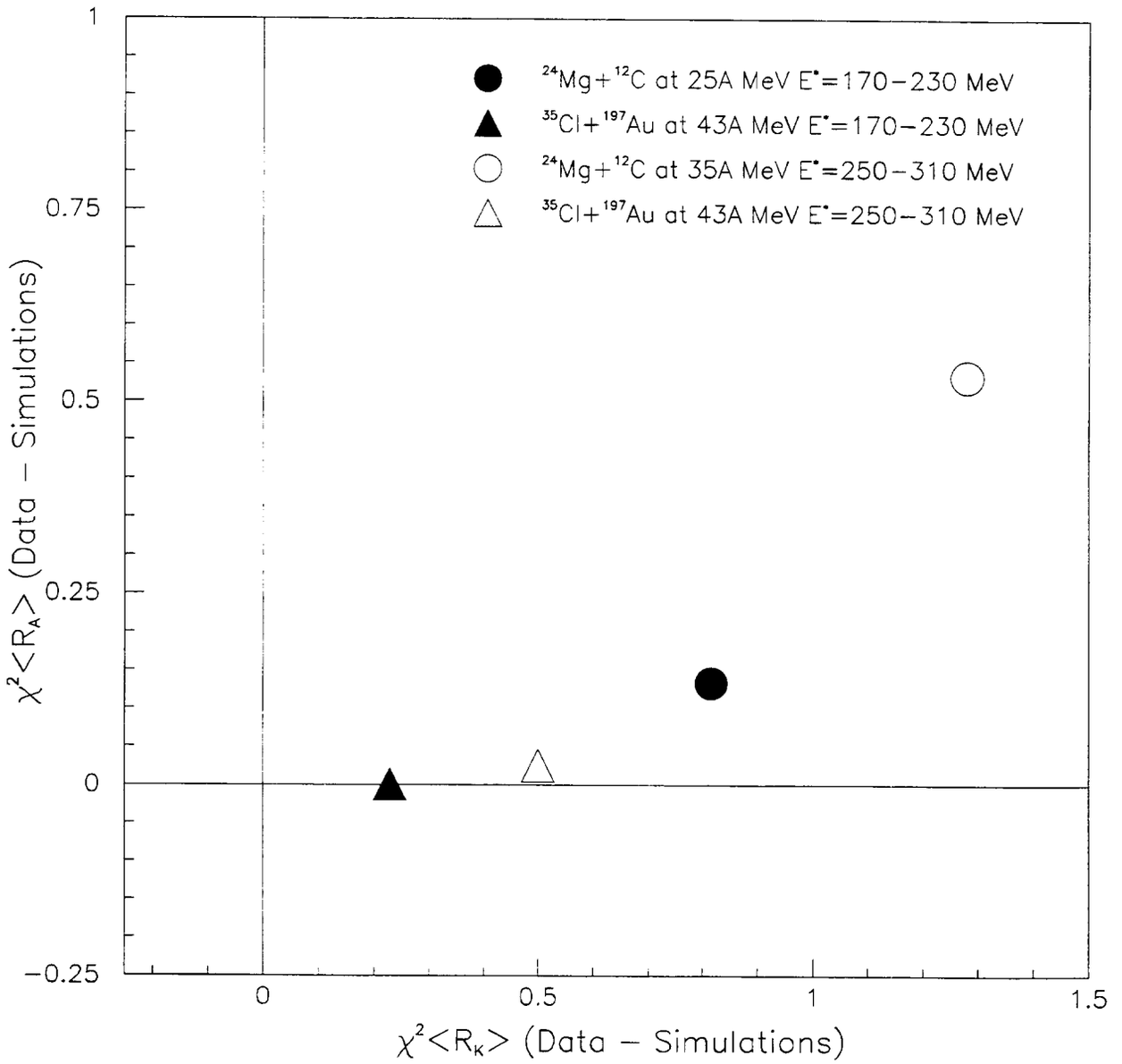

FIG. 13. Y.Larochelle et al.

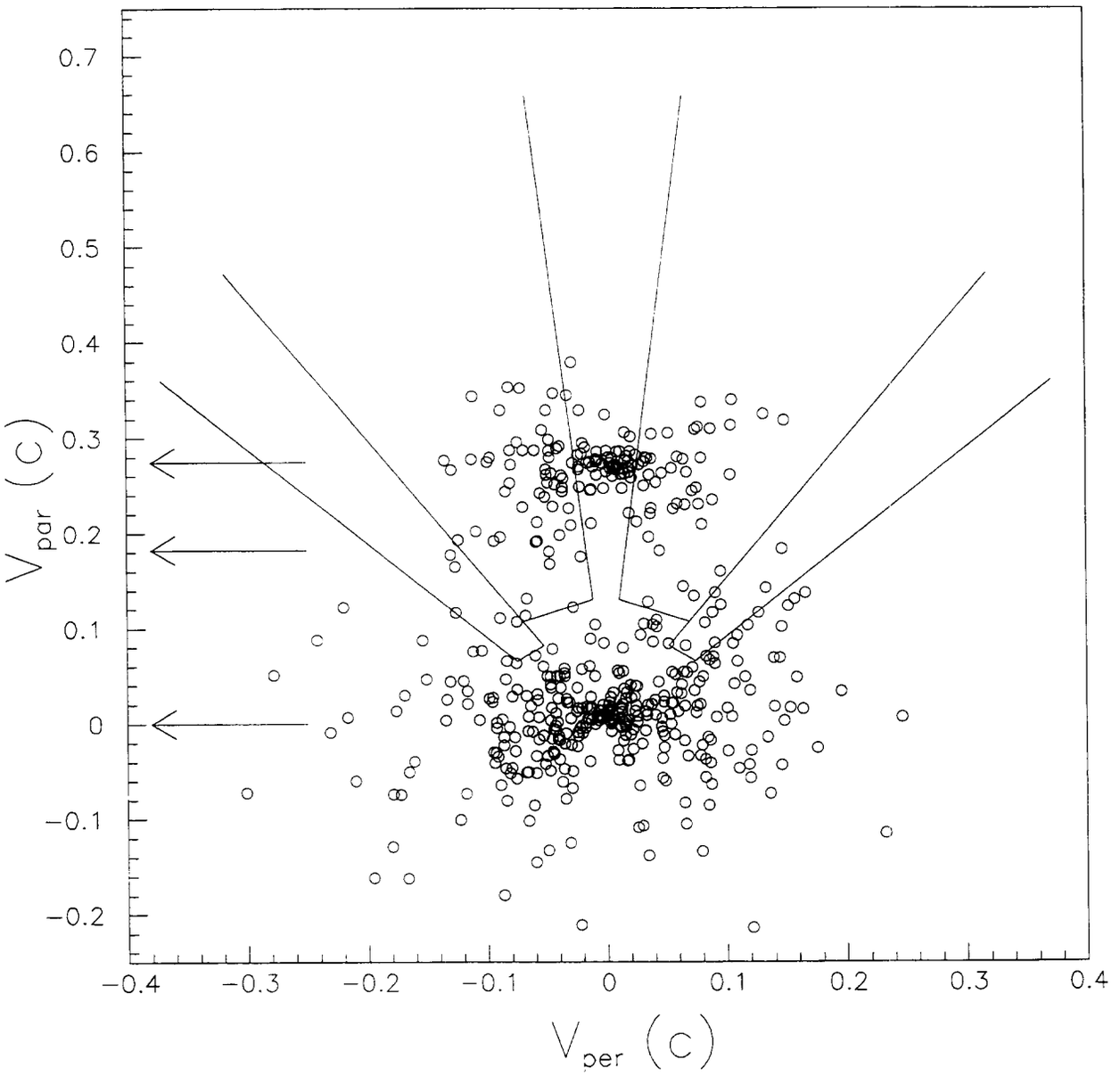

FIG. 14. Y.Larochelle et al.

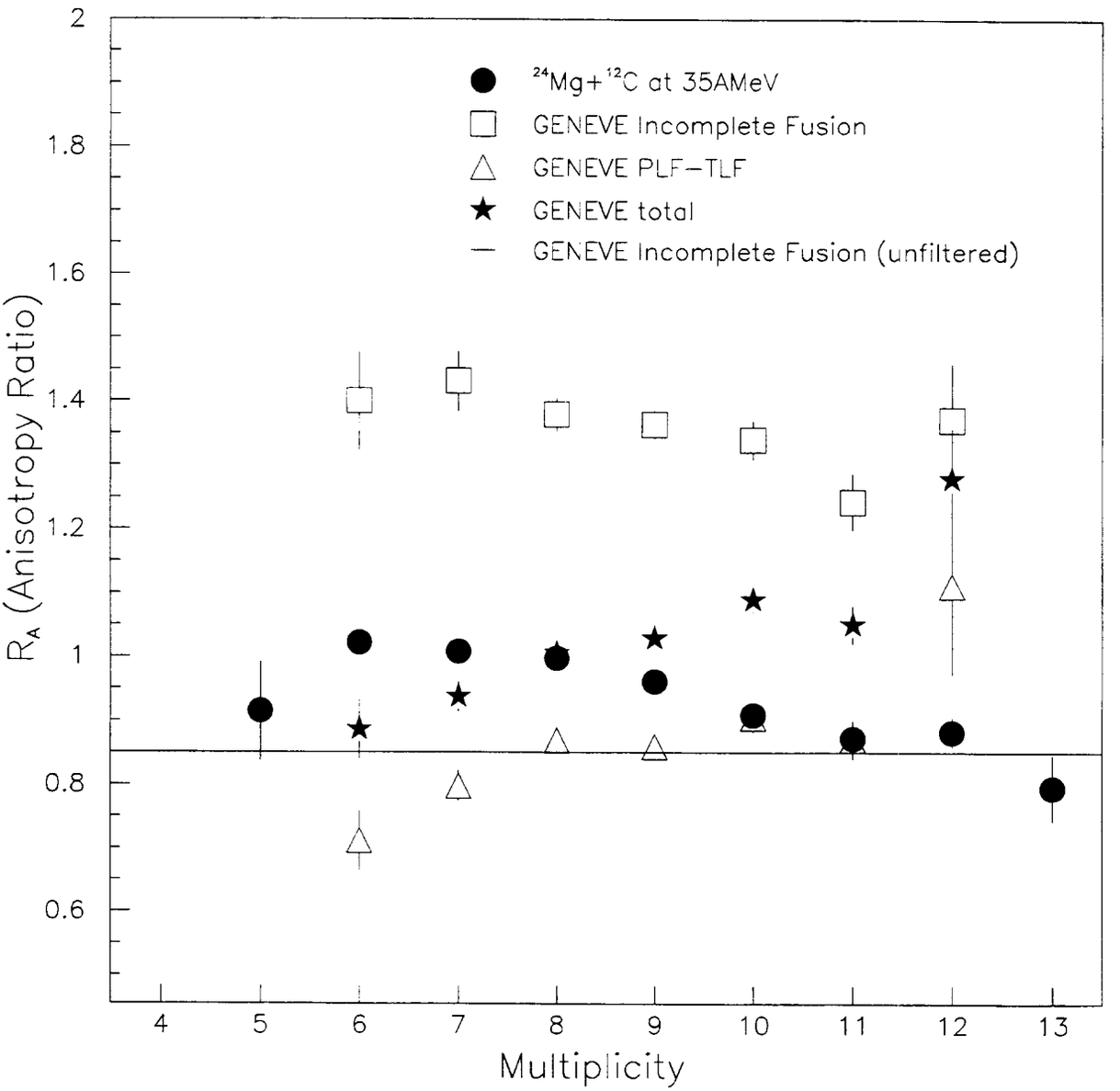

FIG. 15. Y.Larochelle et al.

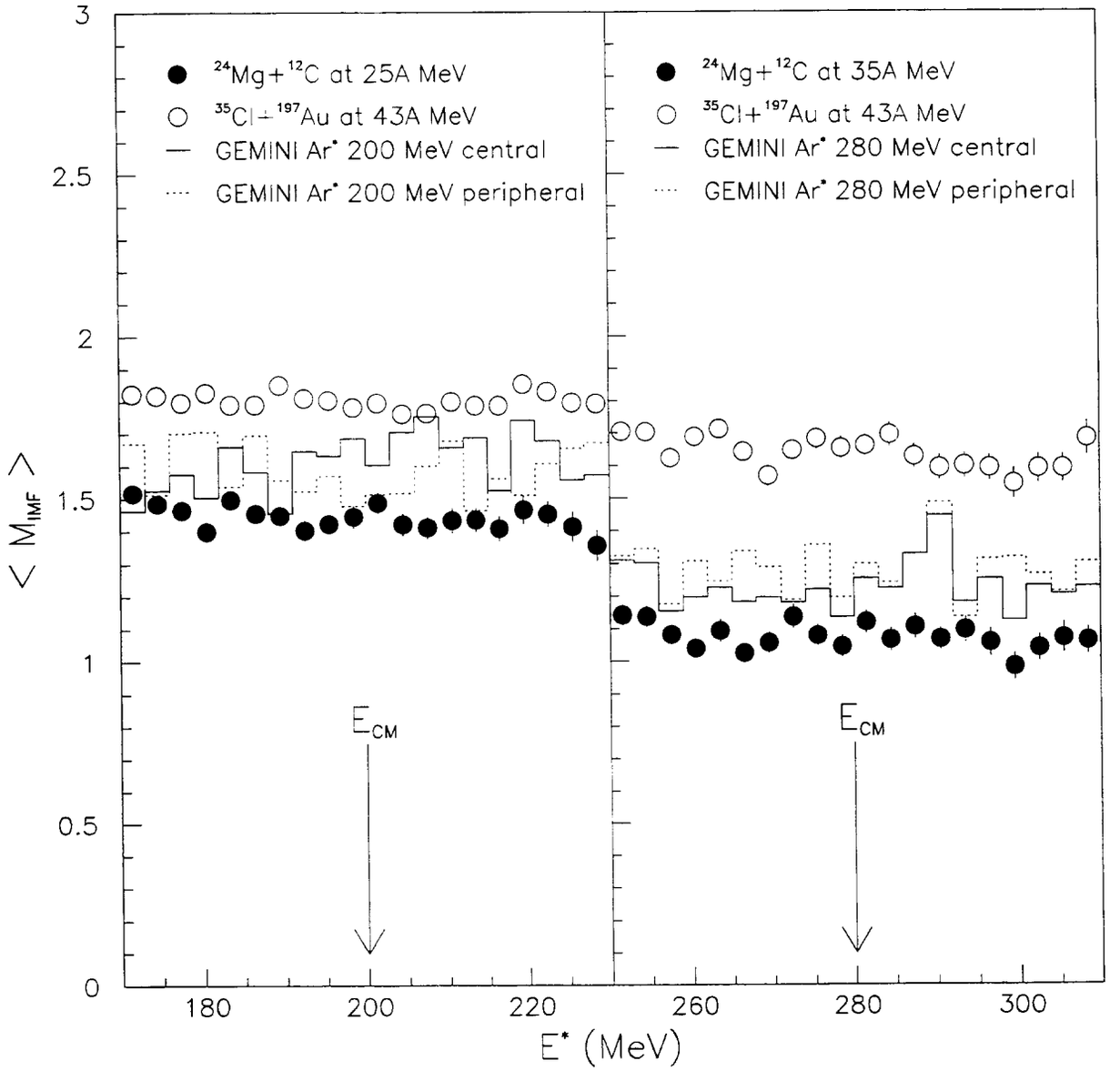

FIG. 16. Y.Larochelle et al.

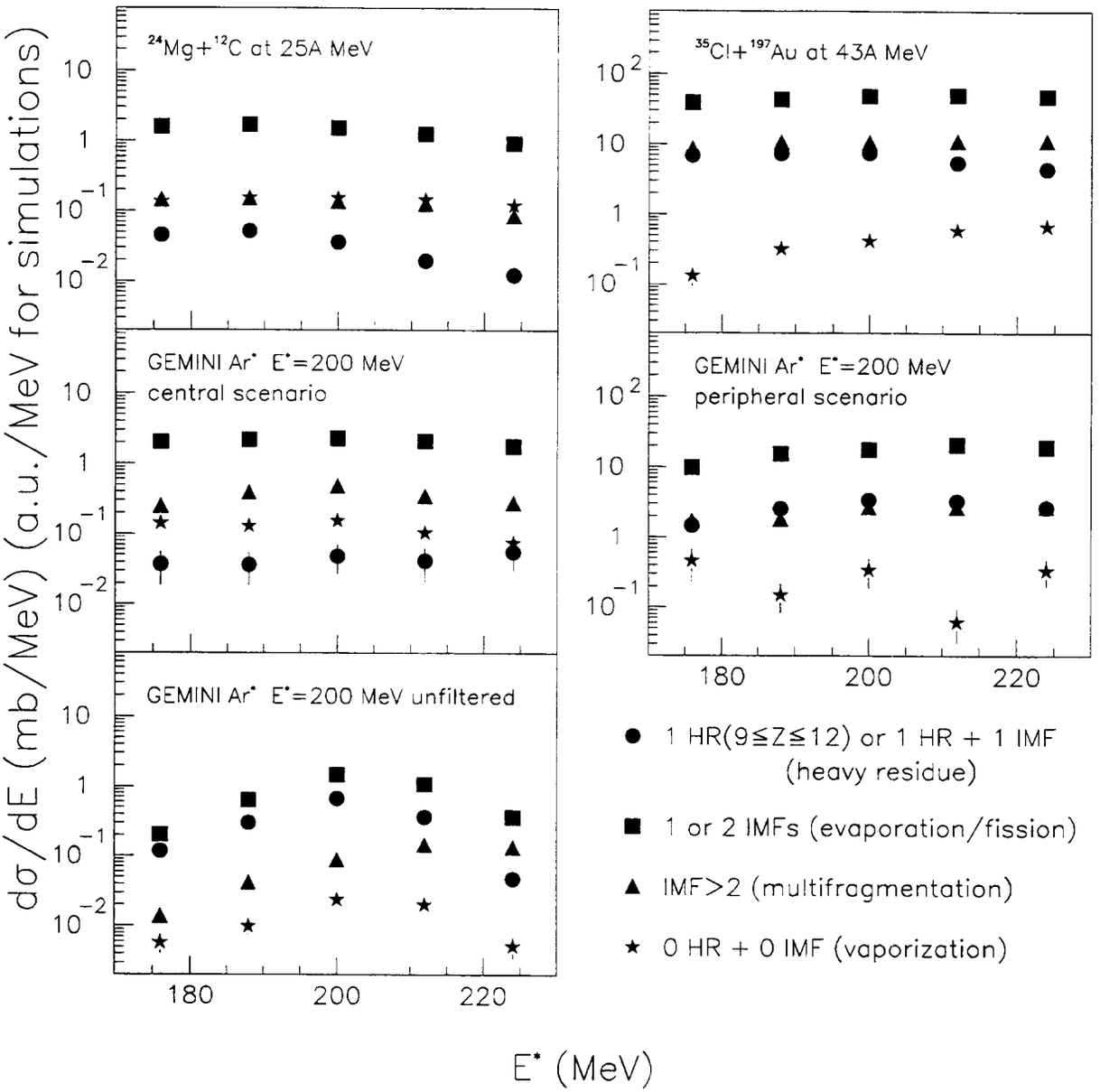

FIG. 17. Y.Larochelle et al.

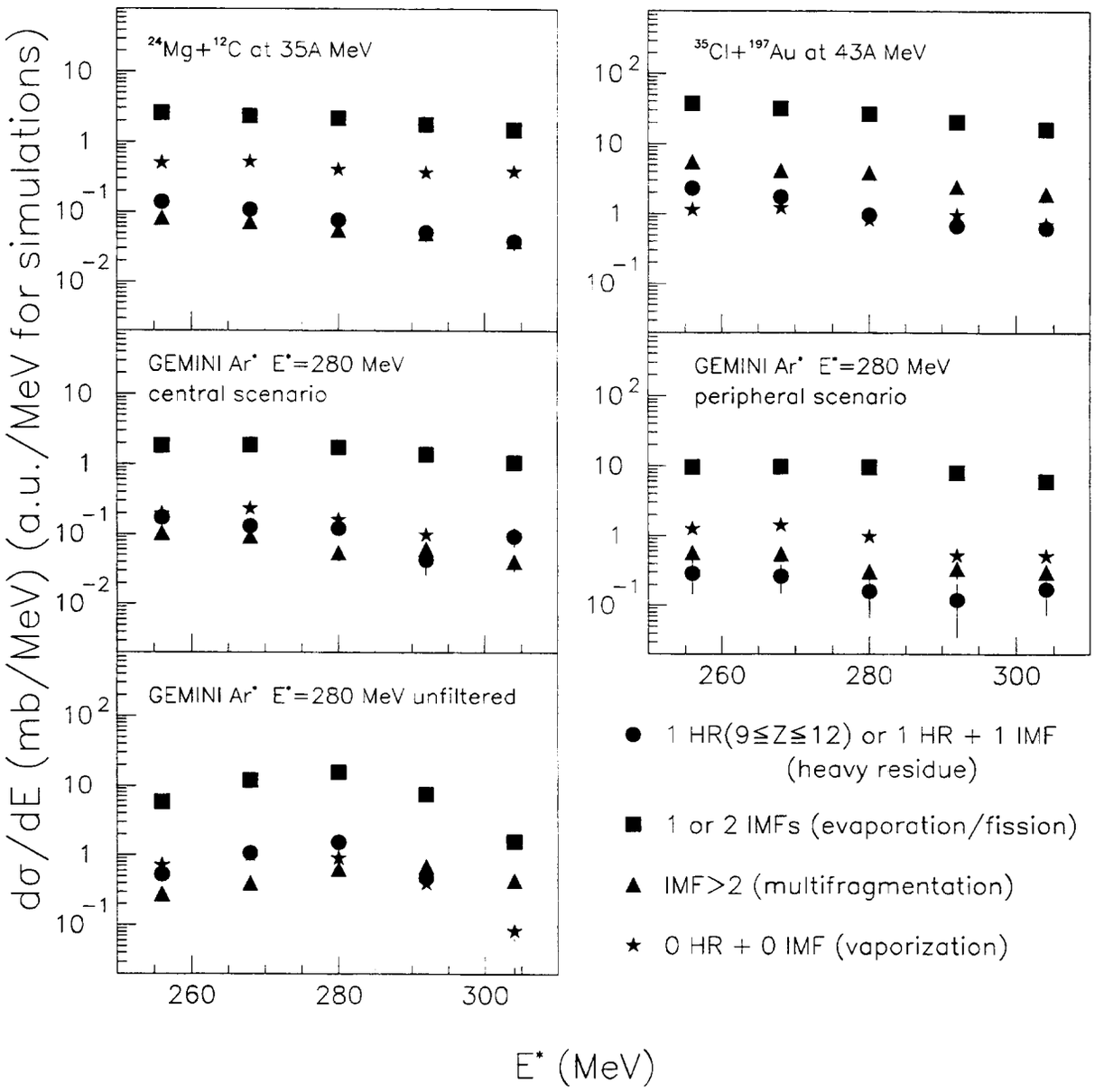

FIG. 18. Y.Larochelle et al.